The DNA damage response relies on the characteristics of ionizing particles in myogenic cells

Haser H. Sutcu[1#*], Arthur Thomas--Joyeux[1], Mikaël Cardot-Martin[2], Delphine Dugué[1], François Vianna[2], Mohamed A. Benadjaoud[3], Marc Benderitter[4], Céline Baldeyron[1*]

[1] Institut de Radioprotection et de Sûreté Nucléaire (IRSN), PSE-SANTE/SERAMED/LRAcc, F-92260, Fontenay-aux-Roses, France

[2] Institut de Radioprotection et de Sûreté Nucléaire (IRSN), PSE-SANTE/SDOS/LMDN, F-13115, Saint-Paul-Lez-Durance, France

[3] Institut de Radioprotection et de Sûreté Nucléaire (IRSN), PSE-SANTE/SERAMED, F-92260, Fontenay-aux-Roses, France

[4] Institut de Radioprotection et de Sûreté Nucléaire (IRSN), PSE-SANTE, F-92260, Fontenay-aux-Roses, France

[#] Present address: Université Paris Cité, Inserm, CEA, Stabilité Génétique Cellules Souches et Radiations/iRCM, F-92265, Fontenay-aux-Roses, France; Université Paris-Saclay, Inserm, CEA, Stabilité Génétique Cellules Souches et Radiations/iRCM, F-92265, Fontenay-aux-Roses, France

* Co-corresponding authors: Céline Baldeyron, celine.baldeyron@irsn.fr; Haser Hasan Sutcu, haser.sutcu@cea.fr

Running title

Ionizing particle specific DDR in muscle cells

Abstract

DNA integrity and stability are vital for proper cellular activity. Nevertheless, to treat cancer patients, DNA is the main target for inducing tumoral cell death. Nowadays, cancer treatment is improving by the development of new technologies, protocols and strategies. Amongst them, the introduction of charged particles as a form of radiotherapy is underway. However, tumor-neighboring healthy tissues are still exposed to ionizing radiations (IR) and subject to late side effects. Skeletal muscle is one of those tissues most likely to be affected. To decipher the DNA damage response (DDR) of skeletal muscle cells, myogenic cells, we irradiated them with microbeams of protons or α-particles and followed the accumulation of DDR proteins at localized irradiation sites. Thereby, we showed that myoblasts, proliferating myogenic cells, repair local IR-induced DNA damage through both non-homologous end-joining and homologous recombination with different recruitment dynamics depending on the characteristics of ionizing particles (type, energy deposition and time after irradiation), whereas myotubes, post-mitotic myogenic cells, display global reduced DNA damage response.

Keywords

Ionizing particle / homologous recombination / microbeam irradiation / non-homologous end-joining / skeletal muscle cells

Introduction

The most common cancer treatments are surgical removal, chemotherapy and radiotherapy, alone or combined depending on the type, grade and localization of cancer (Wang et al, 2018). Although the purpose of these therapies is to get rid of cancerous cells, the therapies themselves give rise to undesired side effects. During radiotherapy, DNA is considered as the main cellular target for biological effects of ionizing radiation (IR) (Han & Yu, 2009). IR produces a wide spectrum of DNA lesions, among which DNA double-strand breaks (DSBs) play a key role in the induction of cell cycle arrest and cell death. Indeed, DSBs are considered to be the most deleterious DNA lesions for genome integrity and stability (Zhao et al, 2020). DSBs can be repaired by four distinct repair pathways in eukaryotic cells: classical non-homologous end-joining (c-NHEJ or NHEJ), homologous recombination (HR), single-strand annealing (SSA), and alternative non-homologous end-joining (alt-NHEJ) (Zhao et al, 2020; van de Kamp et al, 2021). However, NHEJ and HR are the two major mechanisms used for the repair of DSBs, while SSA and alt-NHEJ process the residual DSBs that could not be repaired by NHEJ and HR. While NHEJ is known to be active during the entire cell cycle, HR is limited to S-G2 phases, as it requires template DNA for resynthesis of damaged region guided by homologous sequences on the sister chromatid (Beucher et al, 2009). The principal repair pathway of IR-induced DSBs is reported to be NHEJ (Beucher et al, 2009), which proceeds through KU70/KU80 heterodimer recruitment and formation of DNA-PK complex with DNA-PKcs (DNA-PK catalytic subunit), initiating DNA end-processing, followed by bringing processed DNA broken ends together and ligating by DNA Ligase IV with its cofactors, XRCC4 and XLF/Cernunnos (Nick McElhinny et al, 2000; Ahnesorg et al, 2006). Despite this, the radiosensitivity of cells with deficiency in HR-mediated DSB repair (Grosse et al, 2014; Gerelchuluun et al, 2015; Bright et al, 2019) suggests that HR could also be implicated in the repair of DNA damage induced by low or high linear energy transfer (LET) particles.

Nowadays, along with new technologies, new protocols and modalities of radiotherapy are introduced for preclinical studies and clinical use. Depending on the type and/or invasiveness of cancer to be treated, radiotherapy options range from photon (X-ray, γ-ray)- to charged particle (proton, carbon)-treatments, whether with fractionated (Hua et al, 2008; Nahum, 2015), ablative (Hannan et al, 2022), or flash (Iturri et al, 2023) doses. Today, the 5-year survival rate is 70 % and above for certain types of cancer (e.g. prostate cancer, non-Hodgkin lymphoma, kidney and renal pelvis cancer, ovary cancer, breast cancer) (Siegel et al, 2020). Consequently, along with increased survival rate, late onset side effects of cancer therapies can be seen (Paulino, 2004; Zhang et al, 2015). Accordingly, skeletal muscle (i.e., myofibers), which makes up to approximately 40 % of the body mass (Frontera & Ochala, 2015), is one of the most liable organs to be exposed to IR as an adjacent healthy tissue during radiotherapy. Despite that skeletal muscle tissue is considered to be radioresistant (Olivé et al, 1995; Coquard, 1997), many studies show that, in long term, muscle surrounding the radiotherapy target displays physiological sequelae depending on the dose, frequency, or quality of IR (Cui et al, 2016; D'Souza et al, 2019). Such muscular problems developed upon radiotherapy include muscle wasting, cachexia, contractures, malfunctioning and weakness, and affect the life quality of patient. Moreover, these complications are even more severe for the juvenile patients who are still under development (Kallenbach et al, 2022). Although these side effects could be attenuated by lifestyle, exercise and diet (D'Souza et al, 2019; O'Connor et al, 2022), their causes at the molecular and mechanistic levels are still poorly understood.

Skeletal muscle cells originate from unipotent muscle stem cells (Seale et al, 2001). In developing juvenile organisms muscle stem cells are mostly active and proliferative to contribute for skeletal muscle growth (Gattazzo et al, 2020), whereas in adults, they are quiescent and are called satellite cells (SCs), since they are located at the periphery of myofibers between the basal lamina and the sarcolemma. The SCs only activate for self-renewal, muscle homeostasis and regeneration (Collins et al, 2005). Thus, it is only upon activation that SCs proliferate in the form of myoblast, differentiate and fuse into multi-nucleated myotubes and mature into myofibers (Collins et al, 2005). In order to increase our knowledge of late-onset consequences of radiotherapy on muscle, it is therefore important to assess the efficiency of DNA damage repair mechanisms specific to multi-nucleated myofibers as well as its mono-nuclear precursors cells. This could also give a better understanding for the greater impact of radiotherapies observed on juvenile patients, in which the muscle precursors are still active, unlike in adults. Previously, it has been reported that adult muscle stem cells have more efficient and accurate DNA repair capacity than their committed progeny (Vahidi Ferdousi et al, 2014). Recently, we have also shown that multi-

nucleated skeletal myofibers, generated from muscle stem cells of neonatal mice or immortalized myoblasts, have a reduced DNA damage response (DDR) in comparison to their precursors, myoblasts upon x-ray or α-particle irradiation (Sutcu et al, 2024). Additionally, our previous findings suggest that repair of DSBs induced either by x-ray or α-particle irradiation in mono and multinuclear myogenic cells is essentially carried out by NHEJ (Sutcu et al, 2024) as in their progenitor, muscle stem cells (Vahidi Ferdousi et al, 2014; Sutcu et al, 2023).

Due to the increasing, though still marginal, use of protons (proton therapy) and alpha emitters (nuclear medicine), and based on our recent findings on the DDR in myogenic cells upon α-particle irradiation, we performed a study of the DDR in myogenic cells according to the type and characteristics of ionizing particles delivered and the energy deposited. Therefore, taking advantage of ion microbeam technology (Vianna et al, 2022), we delivered different numbers of 4 MeV protons and 6 MeV α-particles to induce local DNA damage at the sub-nuclear level within nuclei of myogenic cells and we followed the recruitment kinetics of some DDR proteins coupled to GFP throughout myogenic differentiation. Thereby, we found that myoblasts orchestrate IR-induced DSB repair with dynamics that depend on the type of high LET particle used, proton or α-particle, while differentiated myotubes remained with declined DNA damage response as was previously reported (Sutcu et al, 2024).

Results

The dynamic behavior of KU80-GFP at the DNA damage site depends on the type and number of particles delivered.

To assess initial IR-induced DNA damage response of myogenic cells, we used the immortalized murine C2C7 cells stably expressing GFP-tagged proteins involved in DDR: KU80-GFP, 53BP1-GFP and HP1α-GFP (Sutcu et al, 2024). Immunoblot analyses of whole-cell extracts showed that all GFP-tagged proteins used in this study were expressed at least at a one-to-one ratio, or even less (Fig. S1, A) in stably transfected myoblasts and their committed progeny, myotubes. In addition, no free GFP molecules were detected, while a very weak quantity of truncated products for 53BP1-GFP was found in transfected myogenic cells (Fig. S1, A, comparison between upper and lower panels for each protein). To perform *in situ* localized irradiations within the nuclei of living cells, we used the microbeam MIRCOM facility (Bobyk et al, 2022; Sutcu et al, 2024). This microbeam delivers a controlled number of a given particle. Here, we targeted by either 1,000; 200 or 50 α-particles, or 10,000; 2,500 and 500 protons in order to have comparable deposited energy between these two types of particles at the localized irradiation sites (see Materials and methods; Table S1). To investigate the dynamic of NHEJ upon localized α-particle and proton irradiation, we first monitored the accumulation of KU80-GFP protein at the locally irradiated zones over a time frame of 5 min in myoblasts (Fig. 1, A-B) and myotubes (Fig. S1, A-B).

We found that in KU80-GFP-expressing C2C7 cells at the myoblast state, the recruitment of KU80-GFP to DNA damage sites shows similar kinetics upon localized irradiation with 1,000 α-particles (Fig. 1, C) or 10,000 protons (Fig. 1, D), leading to the same deposited energy (Table S1) within the targeted zone. Immediately after irradiation by 1,000 α-particles or 10,000 protons, KU80-GFP accumulated at the sites of DNA damage, reaching a maximum level of recruitment within 60 s followed by its gradual release (Fig. 1, C-D). In contrast, in KU80-GFP-expressing C2C7 cells at the myotube state, we found reduced recruitment of KU80-GFP at the sites of DNA damage induced by a 1,000 α-particles irradiation in comparison to myoblasts (Fig. 1, A and C vs Fig. S1, A and C), as we previously reported (Sutcu et al., 2024). Likewise, we observed that this was also the case upon 10,000 protons irradiation (Fig. 1, B and D vs Fig. S1, B and D), albeit to a lesser extent. We verified that this highly decreased recruitment of KU80-GFP at localized irradiation sites was not due to a lower amount of this protein in myotubes compared to myoblasts (Fig. S1, A and Fig. S2, E).

By reducing the number of particles delivered (i.e., 200 and 50 α-particles or 2,500 and 500 protons), we observed a decrease in the accumulation of KU80-GFP in myoblasts at localized irradiation sites (Fig 1, C-D), transiently reaching to a plateau earlier, followed by its almost immediate release in comparison to irradiations with highest number of particles (i.e., 1,000 α-particles and 10,000 protons). Furthermore, we could observe minor but statistically significant differences in the recruitment kinetics of KU80-GFP according to the number of particles delivered, in particular upon α-particle irradiation (Fig.

1 C-D). In similar pattern, KU80-GFP recruitment in myotubes still remains weaker than in myoblasts even upon lower number of α-particles (Fig. S1, A and C) or protons (Fig. S2, B and D) delivered. Despite lower KU80-GFP accumulation than in myoblasts, whatever the nature and number of particles delivered, KU80-GFP is retained longer at irradiation sites in myotubes (Fig. S1, C and D), and especially upon targeted proton irradiation (Fig. S1, D).

Together, our results show for the first time that in myogenic cells the accumulation and disappearance of KU80-GFP proteins at localized irradiation sites are correlated with the number of particles delivered during irradiation (Fig. 1, C-D), thereby, with the deposited energy and thus, with the number, complexity and clustering of DNA lesions induced (Table S1). Indeed, in myoblasts, the faster disappearance of KU80-GFP upon low number of particle irradiation compared to the one with high number of particles would seem to correlate with amount of induced DNA damage (Table S1) and with fast DSB repair component. On the contrary, in myotubes, reduced but persisting KU80-GFP, which was previously reported to be with high turn-over of KU80 proteins at DNA damage sites (Sutcu et al, 2024), suggests an insufficient amount of KU80 residing on damaged DNA to process the DNA lesions despite its recruitment to the irradiation site. Additionally, absence of other repair pathways; notably HR and declined BER, as demonstrated in (Sutcu et al, 2024), myotubes may have globally weaker DDR than myoblasts, consequently affecting and delaying KU80 dependent DSBR.

The accumulation rate of 53BP1-GFP at DNA damage sites is inversely proportional to the number of particles delivered.

53BP1 is a key protein mediating the signaling of DSBs and orchestrating the choice of DSBR pathways (Bunting et al, 2010), favoring NHEJ by limiting DNA end-resection (Callen et al, 2020). To assess the initial response of 53BP1 to irradiation, we induced local DNA damage by microbeam irradiation within stably 53BP1-GFP-expressing C2C7 cells and monitored its recruitment to micro-irradiation sites in the time frame of 5 min (Fig. 2, A-B).

We demonstrated that there is almost no initial response of 53BP1 in myotubes upon 10,000 protons irradiation (Fig. S3, A and D), strengthening our previous data (Sutcu et al, 2024) showing this near absence of 53BP1 recruitment with 1,000 α-particles. We confirmed that this is not due to a limiting amount of 53BP1-GFP in myotubes (Fig. S1, A and Fig. S3, B). Surprisingly, 50 α-particles triggered a small but significant increase in the initial 53BP1-GFP recruitment to local IR-induced DNA damage sites in myotubes (Fig. S3, A). Even more remarkably, we found in myoblasts that lowering the number of particles to 50 α-particles or to 500 protons induces a recruitment of 53BP1-GFP to irradiation sites almost 2-fold higher than that induced by 1,000 α-particles or 10,000 protons within 5 – 10 min (Fig. 2, A-B). Unlike KU80-GFP, 53BP1-GFP in myoblasts continues to accumulate and does not reach a plateau in this time-frame (Fig. 2 vs Fig. 1).

Therefore, to follow the recruitment of endogenous 53BP1 protein beyond the first 5 -10 min to IR-induced DNA damage sites and compare its kinetics to that of KU80, we immuno-labelled KU80-GFP-expressing cells with antibodies against 53BP1 and the phosphorylated form of the histone variant H2AX (known as γH2AX), used here as a DSB biomarker (Goodarzi & Jeggo, 2012). We thus analyzed their fluorescence intensity at localized site of irradiation. We confirmed in KU80-GFP-expressing myoblasts locally irradiated with 1,000 α-particles or 10,000 protons that 53BP1 recruitment continues to increase at the IR-induced DNA damage sites up to 6 h post-irradiation (Fig. 2, C-D), while KU80-GFP and γH2AX signals gradually and simultaneously disappear (Fig. 2, C). In addition, 1h post-irradiation we found that myoblasts irradiated by 10,000 protons have a higher signal of 53BP1 at irradiation sites than those irradiated by 1,000 α-particles (Fig. 2, D). Decreasing the number of α-particles (i.e., 200 and 50) or protons (i.e., 2,500 and 500) does not seem to reduce the 53BP1 signal detected at irradiation sites 1 h post-irradiation (Fig. 2, E-F), in contrast to the diminishing KU80-GFP and γH2AX signals which correlate with the number of particles used for irradiation (Fig. 2, E) and in line with our above-mentioned kinetics data for KU80-GFP (Fig. 1). At 6 h post-irradiation myoblasts irradiated with 1,000 α-particles show significantly higher 53BP1 intensity at irradiation sites than those irradiated by 10,000 protons (Fig. 2, C). These results indicate that 53BP1 is released faster from chromatin following irradiations with protons than irradiations with α-particles, suggesting that the repair of proton-irradiation-induced DNA damage is performed faster in myoblasts than those induced by α-particle-irradiation, for a same deposited energy at the localized irradiation site.

In contrast, the 53BP1 recruitment to irradiated sites in myotubes is still delayed and reduced even up to 6 h post-irradiation. Moreover, differentiating mono-nuclear cells, designated as myocytes, present an intermediate profile (Fig. S3, C-D vs Fig. 2, D). These results indicate that 53BP1 recruitment to IR-induced DNA lesions is progressively reduced along the myogenic differentiation, reinforcing our previous data (Sutcu et al, 2024).

Taken together, our data show that in myoblasts low particle number induces faster 53BP1 recruitment to localized irradiation sites than high particle number during the initial DDR stages. Then, at 1 h post-irradiation the accumulation of 53BP1 at damaged DNA site is similar, regardless of the number of particles used. Finally, in myoblasts the release of 53BP1 from DNA damage site is faster upon proton-irradiation than upon α-particle-irradiation when the highest numbers of particles are delivered (1,000 α-particles vs 10,000 protons).

NHEJ and HR balance in the processing of ionizing particle-induced DSBs in myoblasts.

Our above-mentioned results show that the early 53BP1 recruitment to damaged DNA site is inversely correlated with the number of particles delivered. As 53BP1 plays a major role in the choice of DSBR pathways (Callen et al, 2020), we next investigated the dynamic behavior of both NHEJ and HR key factors upon localized charged particle irradiation only in myoblasts, as myotubes have no HR activity (Sutcu et al, 2024), which is confirmed by a very low expression level of RAD51 protein in myotubes compared to myoblasts (Fig. S1, B). Therefore, we analyzed in KU80-GFP-expressing C2C7 myoblasts the local enrichment of γH2AX as DSB marker (Goodarzi & Jeggo, 2012) together with the recruitment of KU80-GFP as NHEJ actor, and RAD51 as central and pivotal HR factor (Sung & Robberson, 1995; Baumann & West, 1998), at different time-points after targeted irradiation with protons or α-particles (Fig. 3).

In myoblasts we first observed a pan-nuclear γH2AX staining appearing 1 h after localized irradiation with 1,000 α-particles and being resolved at later time-points (Fig. 3, A). These results are consistent with previous published studies using charged particle irradiation (Meyer et al, 2013; Horn et al, 2015). Furthermore, this pan nuclear signal decreases as the number of delivered particles diminishes and is visible as soon as the number of delivered α-particles reaches 200 (Fig. 3, A). Despite that, to avoid introducing a bias in the quantification of fluorescence signal intensity, we analyzed the whole nuclear γH2AX signal at different time-points after localized irradiation. Accordingly, at each time-point we clearly observed a reduction in the γH2AX signal as a function of deposited energy (Fig. 3, B), directly correlating with a decrease in the number of particles delivered, from 1,000 to 50 α-particles, and with the time elapsed after micro-irradiation, from 1 to 6 h, suggesting the ongoing DSB repair. To confirm the correlation of γH2AX fluorescence intensity with the amount of DNA damage induced by a number of particles targeted, we also assessed the total nuclear γH2AX signal in the C2C7 cells irradiated with intermediate number of α-particles (i.e., 500 and 100 α-particles) (Fig. S3, A). One-hour post-irradiation, we found that the γH2AX signal is indeed the highest after 1,000 α-particles irradiation and it significantly and continuously decreases in a correlated manner with the reduction of the number of particles delivered, from 500 to 50 α-particles (Fig. S4, A).

Within the first 10 minutes after irradiation with 1,000 α-particles the KU80-GFP signal induced at the irradiation site is 5- and 10-fold higher than that induced by a micro-irradiation with 200 and 50 α-particles, respectively (Fig. 3, C-D). Afterwards, the intensity of KU80-GFP signal (Fig. 3, C-D) decreases with a similar pattern to that of γH2AX (Fig. 3, B-C). Six hours post-irradiation with 1,000 α-particles, we observed a clear decrease in KU80-GFP signal at localized DNA damage site. However, the fluorescence signal intensity detected after irradiation with lower number of particles (i.e., 200 and 50 α-particles) at the irradiation site was too weak (under our technical imaging conditions) to distinguish a difference from 1 h post-irradiation (Fig. 3, C-D and Fig. S4, B). Contrary to KU80-GFP, upon irradiation with 1,000 α-particles the RAD51 fluorescence intensity at the localized irradiation site remains relatively low 10 min and 1 h post-irradiation (Fig. 3, C-E). Interestingly, decreasing the number of α-particles from

1,000 to 50 led to an increase in the RAD51 signal intensity at the localized irradiation site, inversely correlating with the KU80-GFP signal and the number of particles delivered (Fig. S4, B).

In addition, in all of the irradiations with α-particles (1,000; 200 or 50 α-particles), the RAD51 signal reaches a maximum, with a fluorescence level 2 folds higher for each condition, 3 h post-irradiation, and then diminishes at the time-point 6 h post-irradiation (Fig. 3, C and E). Additionally, in order to summarize the results obtained in Figures 3 and S4, we performed partial least squares-discriminant analysis (PLS-DA) (Fig. S5, A-B) by taking advantage of measured fluorescence intensities of RAD51 and KU80-GFP at the irradiation sites and of nuclear γH2AX for each individual cell. With these cellular identities, PLS-DA adequately classified the cell groups depending on the active DSBR mechanisms (RAD51 and KU80-GFP recruitments) and dynamics (γH2AX) upon irradiation with different number of α-particles (Fig. S5, A, C and E) and throughout time post-irradiation (Fig. S5, B, D and E). Altogether, our data confirmed that in myoblasts NHEJ is the principal pathway involved in the repair of DSBs induced by α-particles irradiation. However, HR plays an important role at the late DSBR stages, in agreement with a potential switch of DSBR pathways from NHEJ to HR as described in (Shao et al, 2012). Surprisingly, upon local irradiations with low number of α-particles, implication of HR seems to be sooner than for irradiation with 1,000 α-particles.

As DSBR mechanisms depend on the cell cycle (Kakarougkas & Jeggo, 2014), we checked the distribution of myoblats in the cell cycle based on their DNA content by measuring the integrated intensity of DAPI within the cell nuclei (Toledo et al, 2013; Gruel et al, 2016) before and after irradiation (Fig. S4, C-D). The distribution of unirradiated myoblasts in the different phases of the cell cycle at the moment of irradiation was approximately 56.87 ± 5.5% of cells in G1, 3.24 ± 1.5% in S and 13.6 ± 8.7% in G2 (Fig. S4, C). This initial distribution among the cell cycle phases gives the probability of inducing DNA lesions in G1, S, or G2 in myoblasts randomly chosen within the cell monolayer. The targeted myoblasts show 5 - 10 min after irradiation with α-particles (Fig. S4, Di), the similar cell cycle distribution as neighboring non-irradiated myoblasts (Fig. S4, C – 5 - 10 min), 62.3 ± 10.7% of cells in G1, 13,3 ± 10.7% in S and 17.3 ± 10.4% in G2 (Fig. S4, Di – 5 - 10 min). Thus, although in 10 min no obvious change in the cell cycle distribution of irradiated myoblasts is observed, the targeted cells present strong γH2AX and KU80-GFP signals (Fig. 3, 4 and S4). Moreover, while the cell cycle distributions of targeted myoblasts are similar at 1 h and 3 h post-irradiation, showing respectively, 33.7 ± 5.05% and 35.5 ± 8.6% of cells in S /G2 phases, a stage when HR-mediated repair is active, we observed an increase in the mean fluorescence intensity of immunolabelled RAD51 at localized irradiation sites 3 h post-irradiation (Fig. 3, E), compared to that detected 1 h post-irradiation. Together, the cell cycle distribution and PLSA-DA analyses suggest that upon irradiation with α-particles, NHEJ is the initial responding DSBR mechanism and HR-mediated repair occurs with slower kinetics that the contribution of the cell cycle progression alone is not sufficient to fully explain, but may rather be explained by the increased amount of induced DNA lesions of greater complexity.

As differences in DSBR mechanisms and dynamics are observed by reducing energy deposition of α-particles, we therefore investigated and compared the DDR of myoblasts to DNA lesions of different complexities induced by protons. We analyzed at the local irradiation sites the fluorescence intensities of RAD51 and KU80-GFP as well as the nuclear γH2AX signal 5 - 10 min to 6 h post-irradiation with 10,000 protons and 1,000 α-particles, leading to similar deposited energies (Table S1). Upon localized proton irradiation of myoblasts, RAD51 fluorescence intensity reaches its maximum at 1 h post-irradiation, sooner than upon micro-irradiation with α-particles (Fig 4, A). Moreover, the decrease in RAD51 signal at the localized irradiation site is faster upon proton irradiation, starting from 3 h post-irradiation (Fig. 4, A). However, the KU80-GFP recruitment and release kinetics at local DNA damage sites are similar to those observed in myoblasts irradiated with α-particles, but on a smaller scale (Fig. 4, B). Altogether, the faster release of RAD51 and the lower amount of KU80-GFP at the local DNA damage site upon micro-irradiation with 10,000 protons, in comparison to micro-irradiation with 1,000 α-particles (Fig.4, A-B), also in agreement with the faster disappearance of γH2AX signal over time after IR (Fig. 4, C), suggest a faster repair of DNA lesions induced by proton micro-irradiation. Accordingly, the projection of the data obtained in Figure 4 to the previous PLS-DA analysis (Fig. S5) showed distinct scatterplot projections of myoblasts micro-irradiated by protons or α-particles both for the 1 h and 3 h time-points due to strong differences of both KU80-GFP and RAD51 fluorescence identities of cell groups (Fig. S6). The results obtained from the PLS-DA analysis reinforce the idea that the dynamics of

DNA repair mechanisms are different depending on the nature of the particle used for irradiation, but also on the number of particles delivered, despite similar cell cycle distribution of α-particle (Fig. S4, Di) and proton (Fig. S4 Dii) irradiated cells.

Since HR seems to be involved sooner in the process of proton-induced DNA damage repair than that induced by α-particles, we analyzed the behavior of the heterochromatin protein 1 isoform, HP1α. HP1α recruited by p150CAF-1, the largest subunit of histone chaperone chromatin assembly factor 1 (CAF-1), to the site of DNA damage induced by laser micro-irradiation promotes HR (Baldeyron *et al*, 2011). Thus, to further characterize the cellular response to IR, we analyzed the recruitment kinetics of HP1α within stably HP1α-GFP-expressing C2C7 myoblasts upon localized irradiation with 10,000 protons or 1,000 α-particles (Fig. 4, Di). In agreement with our data above (Fig. 4, A), HP1α-GFP recruitment to localized irradiation site is also higher upon proton irradiation than upon α-particle irradiation (Fig. 4, Dii). These results suggest that HR-mediated DSBR takes place earlier upon proton micro-irradiation when compared to α-particle micro-irradiation.

Here we showed that in myoblasts NHEJ is the initial and principal repair pathway to process DNA damage induced by α-particles micro-irradiation and then there is a switch of repair machinery to HR around 3 h post-irradiation. Additionally, decreasing the number of α-particles delivered also favors repair of IR-induced DNA damage by HR. Upon proton irradiation, unlike α-particle-induced DNA damage, both NHEJ and HR seems to be actively involved in the initial stages of DNA damage processing, and at a faster pace.

Discussion

Along with increasing cancer survival rates, the late side effects of radiotherapy treatments on muscle tissue are becoming more apparent (Paulino, 2004; Zhang et al, 2015; Siegel et al, 2020). Muscle is one of healthy neighboring tissue majorly exposed during IR treatment leading to impaired life quality of cancer patients. This is reported to be more severe in pediatric patients who still have an ongoing muscle development (Goodenough *et al*, 2021) and thus their muscle tissue includes all forms of myogenic cells: quiescent, active muscle stem cells; cycling and differentiating precursor cells, myoblasts; and post-mitotic myofibers, as was reported in mice (Gattazzo et al, 2020). Previously we have shown that myotubes have reduced DDR upon irradiation and slower DSB repair capacity in comparison to their precursor cells, myoblasts (Sutcu et al, 2024). However, the repair mechanisms acting in proliferating myoblasts remained poorly characterized. Therefore, to understand why cancer patients suffer from musculoskeletal disorders, and especially why pediatric cancer patients have more severe side effects upon radiotherapy, we investigated the DDR in myogenic cells upon irradiation with different types of charged particles by using ion microbeam technology (Vianna et al, 2022), offering the advantage of delivering controlled number of particles within a sub-nuclear region of cell nucleus. Thereby, we were able to monitor the cellular response to the locally induced DNA damage, particularly by ionizing radiation, while most of the published local DNA damage studies are performed by laser micro-irradiation.

Dose-dependent retention of KU80 at DNA damage site.

We found here that the level of KU80 recruited and retained at the local damage site directly correlates with the number of particles delivered within the nuclei of myoblasts, indicating for the first time that NHEJ-mediated DSB repair can handle increasing amounts of IR-induced DNA lesions.

Additionally, in all conditions of irradiation while myotubes show lower recruitment of KU80 to localized irradiation site in comparison to myoblasts, strengthening the data of our previous work (Sutcu et al, 2024), KU80 in myotubes is retained longer on damaged DNA. One reason for the longer persistence of KU80 at local DNA damage sites in myotubes could be due to the absence of HR repair pathway, as reported in (Vahidi Ferdousi et al, 2014; Sutcu et al, 2024), leaving myotubes entirely dependent on NHEJ to repair IR-induced DSBs, whereas cycling myoblasts still have the capability of deploying HR.

Finally, as previously reported, the recruitment of KU80 occurs in all myogenic cells and its release from DNA may happen when HR takes place to mediate repair of more complex DSBs (Shao et al, 2012; Shibata & Jeggo, 2020). Thus, in myoblasts the faster release of KU80 upon irradiation with smaller number of particles could be either due to generation of smaller number of DSBs rapidly repaired, or

due to the nature of the lesions requiring a potentially earlier switch of DSBR mechanism when NHEJ is not sufficient to cope with the complexity of remaining IR-induced DNA lesions.

Recruitment of 53BP1 correlates with the presence of HR activity in myogenic cells.

53BP1 is a crucial DDR protein, which has multiple roles in DSBR (Shibata & Jeggo, 2020). Generally accepted, the recruitment of 53BP1 to DSBs in proliferative cells promotes DSBR through NHEJ by restricting the 5' DNA end resection and thus preventing the implementation of DSBR mediated by HR (Bunting et al, 2010; Callen et al, 2020). We showed here that 53BP1 recruitment is very low or even almost non-existent at the charged particle irradiation sites in post-mitotic myotubes. This reduced 53BP1 recruitment in myotubes could be the consequence of a general decline in NHEJ along myogenic differentiation, as found above with KU80 (Sutcu et al, 2024). However, we can also hypothesize that in absence of functional HR in myotubes (Sutcu et al, 2024), characterized by a very weak expression of RAD51, 53BP1 is not required, since there is no need to counteract HR implementation to promote NHEJ. Indeed, NHEJ can efficiently occur in absence of 53BP1 for most DSBs (Ward et al, 2004). However, besides its role in the choice of DNA repair pathway, 53BP1 recruitment also induces the chromatin relaxation for the ATM-dependent slow-kinetic DSBR at heterochromatin regions (Noon et al, 2010). Interestingly, it was reported that in myotubes the activity of ATM and its downstream effectors is low (Latella et al, 2004), which would leave the DNA lesions in heterochromatin regions unprocessed or difficult to process. Accordingly, our observations suggest that the very late recruitment of 53BP1 at 6 h post-irradiation would probably provide a protection against unprocessed broken DNA ends, which was reported to be an ATM-independent mechanism (Rybanska-Spaeder et al, 2013). Likewise, although in myoblasts 53BP1 accumulation at DNA damage sites is already higher than in myotubes at the early time-points upon micro-irradiation, it also reaches to its maximum at the later time-points when KU80 becomes undetectable.

Low and delayed recruitment of 53BP1 upon high LET micro-irradiation with high number of charged particles suggests that 53BP1 is potentially dispensable at early stages of DSBR in myogenic cells but it is required at the later stages for the processing of more complex DSBs. However, we have also noticed that 53BP1 accumulation is higher when cells are micro-irradiated with a smaller number of particles, either proton or α-particle. Concurrently, this was also the case with RAD51, suggesting earlier commitment of HR. Recently, sooner implication of HR was also reported in lymphoblastoid cell lines upon exposure to low doses of X-ray irradiation (Mladenov et al, 2022). Moreover, RAD51 recruitment has also been correlated with 53BP1 foci formation in human lung epithelial carcinoma A549 cells upon low doses of X-ray irradiation (Mladenov et al, 2020). Besides, in the absence of p150CAF-1-dependent HP1α recruitment, HR was found to be suppressed as well as the recruitment of 53BP1 to laser micro-irradiation-induced DNA damage sites (Baldeyron et al, 2011). Hence, in agreement with the literature, the direct correlation of RAD51 and 53BP1 recruitment to locally damaged DNA sites upon irradiation with low number of charged particle could implicate 53BP1 in the DNA broken end protection from extensive resection, limiting alternative DSBR pathways (i.e., single strand annealing, SSA, or alternative non-homologous end-joining, alt-NHEJ) (Bakr et al, 2016), and allowing the HR to take over. Indeed, upon localized irradiation with high particle number, unlike strong accumulation of KU80 favoring NHEJ, RAD51 accumulation is delayed to later stages, most likely to process remaining unrepaired DNA broken ends by HR. This could also explain the slow and delayed accumulation of 53BP1 upon micro-irradiation with high number of particles, to protect the unrepaired broken DNA ends until being processed by HR. Thus, although it is contradictory to its generic role in favoring NHEJ, our data imply a novel role for 53BP1 in broken DNA end protection, if not favoring, at least to maintain the DNA ends to be processed by HR. In agreement with this, the unexpected behavior of 53BP1 in myotubes upon local DNA damage induction states that 53BP1 is dispensable in NHEJ-dependent DSBR of myogenic cells.

HR is implicated sooner in the processing of DNA lesions induced by protons, which are also repaired faster.

There are multiple studies pointing out that irradiations with different types of particles (i.e., species, energy and linear energy transfer of particles) induce different kinds of DNA damage (Bertolet et al,

2023) with different levels of complexity (i.e., different types of DNA lesions in the same DNA region) and clustering (i.e., accumulation of DNA damage in the same DNA region) (Nikjoo et al, 2001; Rezaee & Adhikary, 2024). Computational approaches (Nikjoo et al, 2001; Rezaee & Adhikary, 2024) showed that irradiations with α-particles lead to a small number of DNA damage sites with concentrated clusters of complex DNA lesions compared to irradiations with protons, which give a higher number of DNA damage sites containing less clusters of complex DNA lesions. Here, with the use of the MIRCOM ion microbeam, we induce, whatever the particle delivered, protons or α-particles, DNA lesions within a very localized subnuclear area, thus potentially more clustered. We used the computational method called "dsbandrepair" (Meylan et al, 2017; Tuan Anh et al, 2024) for estimating the deposited energy of particles delivered by MIRCOM and the radiation-induced DNA damage yields at irradiation sites within myoblasts. This Monte Carlo-derived simulation tool shows that at comparable deposited energy localized irradiation with α-particles produced 2-fold times DSBs than with protons (Table S1), and the yield of complex DSBs (cDSBs defined as a single DSB with a single or more strand breaks, SBs) is 10 times more with α-particles than with protons (Table S1).

Accordingly, we do detect histone H2AX phosphorylation (γH2AX) only localized at the irradiation sites, suggesting the formation of localized irradiation-induced DSBs. However, after delivering at least 200 α-particles we also observe that H2AX phosphorylation propagates transiently throughout the whole cell nucleus, in addition to a persistent γH2AX signal at the irradiation sites up to 6 h post-irradiation. In agreement with our previous findings (Sutcu et al, 2024) and the literature (Meyer et al, 2013; Horn et al, 2015), this pan-nuclear γH2AX signal is not linked to the induction of apoptosis (Cook et al, 2009) nor to the presence of DSBs, since, like others (Meyer et al, 2013; Horn et al, 2015), we do not find 53BP1 accumulation outside the localized irradiation sites. This pan-nuclear γH2AX is likely due to a stress signal resulting from an increase in indirect DNA lesions induced by the production of reactive species, and/or increase in the complexity and/or clustering of DNA damage generated by charged particle-irradiation (Meyer et al, 2013; Horn et al, 2015; Răileanu et al, 2022; Bertolet et al, 2023). Nevertheless, although this γH2AX signal does not correspond to high LET IR-induced DSBs, it still directly correlates with the number of charged particles delivered during irradiation and its disappearance with the repair of DNA lesions induced by protons or α-particles. Based on our results, we can hypothesize that the pan-nuclear γH2AX signal could serve as a marker of increased complexity and/or clustering of IR-induced DNA lesions, as long as it does not coincide with the induction of apoptosis. Finally, regardless of the type of charged particle, the robust recruitment and the quick release of KU80-GFP at irradiation sites with low number of α-particles or protons suggest that the easy-to-ligate DNA broken-ends are quickly processed by NHEJ. Then, HR processes the remaining complex DNA lesions, with a sooner implication when irradiation is performed with low number of particles.

Furthermore, the faster disappearance of γH2AX signal after proton irradiation, which we have observed to be concomitant with the faster decrease in KU80-GFP and RAD51 signals at targeted irradiation sites suggest that DNA lesions induced by proton is processed faster than the ones induced by α-particle with comparable energy deposition. Our findings agree with simulation studies and our stimulation data suggesting that α-particles induce more complex and clustered DNA damage than protons at comparable deposited energies (Bertolet et al, 2023). While NHEJ is thought as the principal DNA repair mechanism for DNA damage induced by charged particle-irradiation, the importance of HR was also recently reported upon proton irradiation (Vitti & Parsons, 2019). Besides, our data show an earlier recruitment and disappearance of 53BP1 upon proton irradiation, in addition to a higher recruitment of HR-promoting factor HP1α, in comparison to α-particle irradiation in myoblasts. Thus, we confirm that HR is actively involved in the proton-induced DNA damage processing alongside with NHEJ, while it takes place at the later stages upon α-particle irradiation. These results suggest that DNA damage induced by α-particles would require more DNA end-processing by NHEJ before leaving to HR the repair of the remaining DSBs, leading to a slower resolution of the γH2AX signal (Fig. 5). Moreover, a faster DSBR component in myoblasts, despite lower recruitment of KU80-GFP to the DNA damage site upon irradiation with protons than with α-particles also supports our hypothesis that while the repair of α-particle induced DSBs relays on mainly on NHEJ, proton induced DNA damage is processed by more than one mechanism, notably by HR. This could also explain the longer persistence of KU80-GFP at the DNA damage site in HR-deprived myotubes upon irradiation with protons than with α-particles, probably to compensate the lack of HR activity. In conclusion, in proliferating myoblasts the DSBR mechanism engaged depends not only on the deposited energy (i.e., increased number of charged particles), but

also on the type of the charged particle. In general, in myoblasts HR is involved later, potentially to repair unprocessed more complex and/or clustered DNA lesions. However, HR also seems to be more strikingly involved in the repair of DNA damage induced by proton irradiation. Moreover, myogenic cells seem to repair DSBs with distinct mechanisms that adapt and change throughout myogenic differentiation, in which 53BP1 is dispensable in myotubes and in the NHEJ-dependent DSBR of myoblasts (Fig. 5). Future studies based on the inactivation of each pathway would provide a better deciphering of the charged particle-induced DNA damage processing.

Finally, while this study provides further understanding on how skeletal muscle cells respond to different radiation qualities that could be used during radiotherapies, it also points out the importance of considering the neighboring healthy tissue in radiotherapy modalities and treatment planification to be performed on patients. This is even more vital when radiotherapy is particularly combined with chemotherapies, targeting certain DNA damage repair mechanisms and cell cycle control. In that matter, these treatments could also block the recovery of the healthy tissue from induced DNA damage, especially in pediatric patients, who are still physiologically growing and for instance hosting actively cycling myogenic cells apart from differentiated skeletal muscle cells, hence multiple DSBR mechanisms.

Materials and methods

Myogenic cell culture

Immortalized myogenic cells, C2C7 were kindly gifted by Miria Ricchetti (Institut Pasteur, Département de Biologie du Développement et Cellules Souches, Laboratoire de Mécanismes Moléculaires du Vieillissement Pathologique et Physiologique, Paris, France). As previously described in (Sutcu et al, 2024), we maintained the C2C7 cells (Pinset et al, 1988) in myoblast state (proliferative state), by culturing in growth medium (GM) based on DMEM Glutamax (Gibco) supplemented with 20 % fetal calf serum (FCS, Eurobio), and 100 $U.mL^{-1}$ penicillin and 100 $\mu g.mL^{-1}$ streptomycin (i.e., 1 % P/S; Gibco). To generate post-mitotic myotubes, once myoblasts have reached 80 % confluency, we switched the medium to differentiation medium (DM) corresponding to phenol-red free DMEM (Gibco) complemented with 2 % horse serum (HS, Gibco), 1 % P/S, 1% Glutamax (Gibco), and 1% Sodium Pyruvate (Gibco). To note, 50 % of DM was refreshed after 3 days and every consecutive day after. We incubated all the cells in a humidified atmosphere at 37 °C with 5 % CO_2 and 3 % O_2.

During irradiation experiments on MIRCOM platform, we grew immortalized C2C7 myoblasts and their committed progenies, myotubes on 4 µm thick polypropylene foil (Goodfellow) pre-coated with 10 $ng.\mu L^{-1}$ of Cell-Tak (Corning) followed by 10 % Matrigel (Corning) in DMEM on special PEEK dishes, as described in (Vianna et al, 2022). On the day of irradiation, we replaced the GM medium with phenol-red free version to reduce potential autofluorescence.

Plasmids and transfections

The plasmids expressing GFP-tagged protein of interest were kindly provided by Pascale Bertrand (53BP1-GFP; CEA, iRCM/IBFJ, UMRE008 Stabilité Génétique, Cellules Souches et Radiations, Fontenay-aux-Roses, France), Dik C. van Gent (KU80-GFP; Erasmus MC, Departments of Cell Biology and Genetics, Rotterdam, The Netherlands), and G. Almouzni (HP1α-GFP; Institut Curie, UMR3664 Dynamique du Noyau, Paris, France). As previously described in (Sutcu et al, 2024), these plasmids were transfected in C2C7 myoblasts with TurboFect (ThermoFisher Scientific) according to the manufacturer's instructions. To get successful transfection, C2C7 cells were transfected 1-day post-seeding at about 50 % - 60 % confluency. Then, to obtain stable and homogenous GFP-tagged protein expressing C2C7 lines, 24 h post-transfection the GFP-expressing cells were enriched under $1mg.mL^{-1}$ of geneticin (G418 sulfate; Gibco) selection for 10 consecutive days. Then, the GFP-tagged protein expressing C2C7 cells were isolated by FACs sorting and further expanded (Sutcu *et al.*, 2024). To note, GFP-tagged protein expressing myotubes were obtained by inducing differentiation of their precursors, GFP-tagged protein expressing myoblasts.

508 ## *MIRCOM, Microbeam particle irradiation*

509 We performed the localized irradiation of samples by 4 MeV protons, or 6 MeV α-particles generated
510 from hydrogen and helium ions, respectively, by using the MIRCOM facility, operated by the Institute for
511 Radiological Protection and Nuclear Safety (IRSN) in Cadarache, France (Vianna et al, 2022). This
512 facility is equipped with a focused ion microbeam, which is produced by a 2 MV Tandetron™ accelerator
513 manufactured by High Voltage Engineering Europa B.V. (HVEE, Amersfoort, The Netherlands). It has
514 been designed to perform in-air targeted micro-irradiation of living biological samples with a controlled
515 number of ions and a targeting accuracy of 2.1 ± 0.7 µm with a beam spot diameter of a few micrometers
516 (Vianna et al, 2022).

517 As protons and α-particles have low penetration capacity and thus short travel distance through matter,
518 the cells are seeded in a specific PEEK cell dish with a 4 µm thick polypropylene foil (Goodfellow)
519 (Vianna et al, 2022). The LET of the particles at the entrance of the samples after going through the
520 extraction window (150 nm), a residual air layer (250 µm), and the polypropylene foil (4 µm) is 84 keV.µm^{-}
521 ^{1} for 6 MeV α-particles (Bobyk et al, 2022) and 10 keV.µm^{-1} for 4 MeV protons, calculated with SRIM
522 (Vianna et al, 2022). Thus, by using the computational method called "dsbandrepair" (Table S1), we
523 estimated the specific energy deposited within the targeted volume, and it is approximately 35,04 keV
524 for one 4 MeV proton and 346,2 keV for one 6 MeV α-particle in our experimental conditions of localized
525 irradiation. The minimum number of particles targeted is fixed to 50 α-particles and 500 protons, since
526 it is the minimum particle number allowing the detection of RAD51 recruitment under our experimental
527 conditions (data not shown).

528 During irradiation, myogenic cells are placed under an inverted epifluorescence microscope
529 (AxioObserver™ Z1, Carl Zeiss Microscopy GmbH, Jena, Germany) within a 37 °C heating chamber.
530 The relevant nuclei of GFP-expressing cells are identified and selected for irradiation with a 20x
531 objective (Zeiss LD Plan-NEOFLUAR 20x/0.4 Korr). Then, we targeted the nuclei of selected myogenic
532 cells with the indicated number of protons or α-particles, which was determined by the definition of an
533 opening time of the microbeam on each target, as described previously (Bobyk et al, 2022; Vianna et
534 al, 2022; Sutcu et al, 2024). Thus, the energy deposition of each irradiation with protons or α-particles
535 is directly correlated to the number of particles delivered (Table S1).

536 To follow the recruitment kinetics of our GFP-tagged proteins of interest, we started time-lapse imaging
537 10 s before targeted irradiation with the indicated number of particles and recorded images every 2 s
538 with a monochromatic AxioCam™ MRm rev. 3 CCD camera (Carl Zeiss Microscopy GmbH, Germany)
539 using the CRionScan software (Vianna et al, 2022). We recorded images with an exposure time of 800
540 ms. In total, we kept myogenic cells in the microbeam chamber for less than 30 min.

541 ## *Immunostaining and image acquisition*

542 At the indicated time following irradiation, myogenic cells were fixed with 2 % paraformaldehyde (PFA;
543 EMS, Euromedex) in phosphate-buffered saline (PBS; Gibco) for 20 min, and then permeabilized with
544 0.5 % Triton X-100 (Sigma-Aldrich) in PBS for 5 min. To increase the stringency cells were washed with
545 0.1% Tween 20 (Sigma-Aldrich) in PBS (PBS-T), then blocked with 5% BSA (Sigma-Aldrich) in PBS-T.
546 Next, myogenic cells were incubated with the indicated primary antibodies overnight at 4°C. After three
547 washes in PBS-T, the cells were incubated with the appropriate fluorophore-conjugated secondary
548 antibodies for 1 h at room temperature (RT). After three washes in PBS-T, myogenic cells were incubated
549 with 0.5 µg/mL DAPI (Molecular Probes) in PBS for 5 min at RT. Finally, after three washes in PBS,
550 myogenic cells on polypropylene foil were mounted between slide and coverslip with Prolong Diamond
551 antifade mounting medium (Molecular Probes). The myogenic cells were imaged with C-Plan
552 Apochromat 63x/1.4 Oil DIC M27 objective under a LSM 780 NLO confocal microscope, piloted with the
553 Zen Black 2011 SP4 software (Carl Zeiss MicroImaging GmbH, Germany).

554 ## *Antibodies*

555 Primary antibodies used during immunofluorescence experiments are: rabbit anti-53BP1 (Bio-Techne,
556 Novus Biologicals, NB 100-304; 1:500); mouse anti-γH2AX (Millipore, UpState, 05-636; 1:2,000); rabbit
557 anti-RAD51 (Abcam, ab137323; 1:400).

Secondary antibodies used are: donkey anti-mouse or donkey anti-rabbit coupled to Alexa Fluor 594 or 647 (Invitrogen, ThermoFisher Scientific; 1:1,000). To amplify the GFP fluorescence intensity post-fixation, we used GFP booster nanobodies conjugated with Alexa fluor 488 (Chromotek, gb2AF488; 1:500).

Quantification and Statistical analyses

The data shown result from at least two independent experiments.

All the images were processed, analyzed, and quantified by ImageJ software (version 1.53e) (Schneider et al, 2012), and statistical analyses were performed by Prism software (version 9; GraphPad Inc.) and Excel (Microsoft).

As previously described (Sutcu et al, 2024), in order to quantify the fluorescence re-localization of GFP-tagged proteins observed by time-lapse imaging upon MIRCOM irradiation, we manually selected and followed regions of interest (ROI). We measured the mean intensity of ROIs in every image and plotted them against time. To obtain the relative intensity of GFP-tagged repair proteins recruited at the irradiation site, the mean intensity of non-irradiated site was subtracted from ROIs and normalized to mean fluorescence intensity of total nuclei. Then the obtained data were corrected for non-specific fluorescence bleaching and normalized for the fluorescence intensity measured before irradiation.

Fluorescence intensity analysis over time-points post-fixation was performed in a similar manner to time-lapse image analysis, as described above, on immunolabeled samples. The relative fluorescence intensity of immunolabeled proteins recruited to the irradiation site was obtained by subtracting the mean intensity of non-irradiated sites from the mean intensity of regions of interest (ROIs, irradiated site) — of the same size across all conditions — and normalizing to the mean fluorescence intensity of total nuclei. As a marker of DSB, the appearance and disappearance of the phosphorylation of histone variant H2AX upon induced DNA damage were analyzed over time. Specifically, we measured the mean intensity of immunolabeled γH2AX in the entire irradiated nucleus, minus background intensity.

All statistical analyses were performed from at least 3 independent experiments. The smoothing and comparison between the kinetic curves of KU80-GFP and 53BP1-GFP recruitment under different irradiation conditions were performed within the generalized additive models (GAM) framework (Hastie & Tibshirani, 1995) where the smoothing of the KU80-GFP time-kinetic data was performed using penalized splines. The statistical inference on the difference between two kinetic curves was based on the uncertainties of the smoothing process: a difference at a given time-point was considered as significant if its associated confidence interval did not contain zero. This approach permitted us to highlight the significant differences along the time-point values.

Author Contributions

HHS: Conceptualization, Data curation, Formal Analysis, Investigation, Methodology, Project administration, Validation, Visualization, Writing – original draft. **ATJ** and **DD:** Investigation, Methodology. **MCM:** Methodology (α-particle and proton irradiation experiments). **FV:** Methodology, Supervision (α-particle and proton irradiation experiments). **MAB:** Formal Analysis. **MB:** Supervision, Validation. **CB:** Formal analysis, Funding acquisition, Project administration, Supervision, Validation, Visualization, Writing – original draft.

All authors read and approved the final manuscript.

Acknowledgments

The authors thank the PSE-SANTE/SDOS/LMDN team of the IRSN for their excellent technical expertise on the MIRCOM facility and Valérie Buard (PSE-SANTE/SERAMED/LRMed) for her technical support on the IRSN confocal microscopy facility. The authors are grateful to P. Radicella for his critical reading of the manuscript, and to G. Gruel for his helpful suggestions.

Funding

This work was supported by Institute National du Cancer, France (Grant number: PLBIO19-126 LS194750 INCa 2019).

Data Availability Statement

The source data for the main and supplemental figures are available in the published article and its online supplemental files.

Conflict of Interest Statement

The authors declare that they have no conflict of interest.

References

Ahnesorg P, Smith P, Jackson SP (2006) XLF interacts with the XRCC4-DNA ligase IV complex to promote DNA nonhomologous end-joining. *Cell* 124: 301–313. doi:10.1016/j.cell.2005.12.031.

Bakr A, Köcher S, Volquardsen J, Petersen C, Borgmann K, Dikomey E, Rothkamm K, Mansour WY (2016) Impaired 53BP1/RIF1 DSB mediated end-protection stimulates CtIP-dependent end resection and switches the repair to PARP1-dependent end joining in G1. *Oncotarget* 7: 57679–57693.

Baldeyron C, Soria G, Roche D, Cook AJ, Almouzni G (2011) HP1alpha recruitment to DNA damage by p150CAF-1 promotes homologous recombination repair. *J Cell Biol* 193: 81–95. doi:10.1083/jcb.201101030.

Baumann P, West SC (1998) Role of the human RAD51 protein in homologous recombination and double-stranded-break repair. *Trends Biochem Sci* 23: 247–251. doi:10.1016/s0968-0004(98)01232-8.

Bertolet A, Chamseddine I, Paganetti H, Schuemann J (2023) The complexity of DNA damage by radiation follows a Gamma distribution: insights from the Microdosimetric Gamma Model. *Front Oncol* 13: 1196502. doi:10.3389/fonc.2023.1196502.

Beucher A, Birraux J, Tchouandong L, Barton O, Shibata A, Conrad S, Goodarzi AA, Krempler A, Jeggo PA, Löbrich M (2009) ATM and Artemis promote homologous recombination of radiation-induced DNA double-strand breaks in G2. *EMBO J* 28: 3413–3427. doi:10.1038/emboj.2009.276.

Bobyk L, Vianna F, Martinez JS, Gruel G, Benderitter M, Baldeyron C (2022) Differential Recruitment of DNA Repair Proteins KU70/80 and RAD51 upon Microbeam Irradiation with α-Particles. *Biol Basel* 11. doi:10.3390/biology11111652.

Bright SJ, Flint DB, Chakraborty S, McFadden CH, Yoon DS, Bronk L, Titt U, Mohan R, Grosshans DR, Sumazin P *et al* (2019) Nonhomologous End Joining Is More Important Than Proton Linear Energy Transfer in Dictating Cell Death. *Int J Radiat Oncol Biol Phys* 105: 1119–1125.

Bunting SF, Callén E, Wong N, Chen HT, Polato F, Gunn A, Bothmer A, Feldhahn N, Fernandez-Capetillo O, Cao L *et al* (2010) 53BP1 inhibits homologous recombination in Brca1-deficient cells by blocking resection of DNA breaks. *Cell* 141: 243–254. doi:10.1016/j.cell.2010.03.012.

Callen E, Zong D, Wu W, Wong N, Stanlie A, Ishikawa M, Pavani R, Dumitrache LC, Byrum AK, Mendez-Dorantes C *et al* (2020) 53BP1 Enforces Distinct Pre- and Post-resection Blocks on Homologous Recombination. *Mol Cell* 77: 26-38 e7. doi:10.1016/j.molcel.2019.09.024.

Collins CA, Olsen I, Zammit PS, Heslop L, Petrie A, Partridge TA, Morgan JE (2005) Stem cell function, self-renewal, and behavioral heterogeneity of cells from the adult muscle satellite cell niche. *Cell* 122: 289–301. doi:10.1016/j.cell.2005.05.010.

Cook PJ, Ju BG, Telese F, Wang X, Glass CK, Rosenfeld MG (2009) Tyrosine dephosphorylation of H2AX modulates apoptosis and survival decisions. *Nature* 458: 591–596. doi:10.1038/nature07849.

Coquard R (1997) [Late effects of radiotherapy on the skeletal muscle]. *Cancer Radiother* 1: 790–791.

Cui W, Bennett AW, Zhang P, Barrow KR, Kearney SR, Hankey KG, Taylor-Howell C, Gibbs AM, Smith CP, MacVittie TJ (2016) A non-human primate model of radiation-induced cachexia. *Sci Rep* 6: 23612. doi:10.1038/srep23612.

D'Souza D, Roubos S, Larkin J, Lloyd J, Emmons R, Chen H, De Lisio M (2019) The Late Effects of Radiation Therapy on Skeletal Muscle Morphology and Progenitor Cell Content are Influenced by Diet-Induced Obesity and Exercise Training in Male Mice. *Sci Rep* 9: 019–43204.

Frontera WR, Ochala J (2015) Skeletal muscle: a brief review of structure and function. *Calcif Tissue Int* 96: 183–195. doi:10.1007/s00223-014-9915-y.

Gattazzo F, Laurent B, Relaix F, Rouard H, Didier N (2020) Distinct Phases of Postnatal Skeletal Muscle Growth Govern the Progressive Establishment of Muscle Stem Cell Quiescence. *Stem Cell Rep* 15: 597–611. doi:10.1016/j.stemcr.2020.07.011.

Gerelchuluun A, Manabe E, Ishikawa T, Sun L, Itoh K, Sakae T, Suzuki K, Hirayama R, Asaithamby A, Chen DJ *et al* (2015) The major DNA repair pathway after both proton and carbon-ion radiation is NHEJ, but the HR pathway is more relevant in carbon ions. *Radiat Res* 183: 345–356. doi:10.1667/rr13904.1.

Goodarzi AA, Jeggo PA (2012) Irradiation induced foci (IRIF) as a biomarker for radiosensitivity. *Mutat Res* 736: 39–47. doi:10.1016/j.mrfmmm.2011.05.017.

Grosse N, Fontana AO, Hug EB, Lomax A, Coray A, Augsburger M, Paganetti H, Sartori AA, Pruschy M (2014) Deficiency in homologous recombination renders Mammalian cells more sensitive to proton versus photon irradiation. *Int J Radiat Oncol Biol Phys* 88: 175–181. doi:10.1016/j.ijrobp.2013.09.041.

Gruel G, Villagrasa C, Voisin P, Clairand I, Benderitter M, Bottollier-Depois J-F, Barquinero JF (2016) Cell to Cell Variability of Radiation-Induced Foci: Relation between Observed Damage and Energy Deposition. *PLOS ONE* 11: e0145786. doi:10.1371/journal.pone.0145786.

Han W, Yu KN (2009) Response of cells to ionizing radiation. In Advances in Biomedical Sciences and Engineering, pp. 204–262.

Hannan R, Christensen M, Christie A, Garant A, Pedrosa I, Robles L, Mannala S, Wang C, Hammers H, Arafat W *et al* (2022) Stereotactic Ablative Radiation for Systemic Therapy-naïve Oligometastatic Kidney Cancer. *Eur Urol Oncol* 5: 695–703. doi:10.1016/j.euo.2022.06.008.

Hastie T, Tibshirani R (1995) Generalized additive models for medical research. *Stat Methods Med Res* 4: 187–196. doi:10.1177/096228029500400302.

Horn S, Brady D, Prise K (2015) Alpha particles induce pan-nuclear phosphorylation of H2AX in primary human lymphocytes mediated through ATM. *Biochim Biophys Acta* 1853: 2199–2206. doi:10.1016/j.bbamcr.2015.06.010.

Hua C, Gray JM, Merchant TE, Kun LE, Krasin MJ (2008) Treatment planning and delivery of external beam radiotherapy for pediatric sarcoma: the St. Jude Children's Research Hospital experience. *Int J Radiat Oncol Biol Phys* 70: 1598–1606. doi:10.1016/j.ijrobp.2007.12.013.

Iturri L, Bertho A, Lamirault C, Juchaux M, Gilbert C, Espenon J, Sebrie C, Jourdain L, Pouzoulet F, Verrelle P *et al* (2023) Proton FLASH Radiation Therapy and Immune Infiltration: Evaluation in an Orthotopic Glioma Rat Model. *Int J Radiat Oncol Biol Phys* 116: 655–665.

Kakarougkas A, Jeggo PA (2014) DNA DSB repair pathway choice: an orchestrated handover mechanism. *Br J Radiol* 87: 20130685. doi:10.1259/bjr.20130685.

Kallenbach JG, Bachman JF, Paris ND, Blanc RS, O'Connor T, Furati E, Williams JP, Chakkalakal JV (2022) Muscle-specific functional deficits and lifelong fibrosis in response to paediatric radiotherapy and tumour elimination. *J Cachexia Sarcopenia Muscle* 13: 296–310. doi:10.1002/jcsm.12902.

van de Kamp G, Heemskerk T, Kanaar R, Essers J (2021) DNA Double Strand Break Repair Pathways in Response to Different Types of Ionizing Radiation. *Front Genet* 12.

Latella L, Lukas J, Simone C, Puri PL, Bartek J (2004) Differentiation-induced radioresistance in muscle cells. *Mol Cell Biol* 24: 6350–6361. doi:10.1128/mcb.24.14.6350-6361.2004.

Meyer B, Voss KO, Tobias F, Jakob B, Durante M, Taucher-Scholz G (2013) Clustered DNA damage induces pan-nuclear H2AX phosphorylation mediated by ATM and DNA-PK. *Nucleic Acids Res* 41: 6109–6118. doi:10.1093/nar/gkt304.

Meylan S, Incerti S, Karamitros M, Tang N, Bueno M, Clairand I, Villagrasa C (2017) Simulation of early DNA damage after the irradiation of a fibroblast cell nucleus using Geant4-DNA. *Sci Rep* 7: 11923. doi:10.1038/s41598-017-11851-4.

Mladenov E, Paul-Konietzko K, Mladenova V, Stuschke M, Iliakis G (2022) Increased Gene Targeting in Hyper-Recombinogenic LymphoBlastoid Cell Lines Leaves Unchanged DSB Processing by Homologous Recombination. *Int J Mol Sci* 23. doi:10.3390/ijms23169180.

Mladenov E, Staudt C, Soni A, Murmann-Konda T, Siemann-Loekes M, Iliakis G (2020) Strong suppression of gene conversion with increasing DNA double-strand break load delimited by 53BP1 and RAD52. *Nucleic Acids Res* 48: 1905–1924. doi:10.1093/nar/gkz1167.

Nahum AE (2015) The radiobiology of hypofractionation. *Clin Oncol R Coll Radiol* 27: 260–269. doi:10.1016/j.clon.2015.02.001.

Nick McElhinny SA, Snowden CM, McCarville J, Ramsden DA (2000) Ku recruits the XRCC4-ligase IV complex to DNA ends. *Mol Cell Biol* 20: 2996–3003. doi:10.1128/mcb.20.9.2996-3003.2000.

Nikjoo H, O'Neill P, Wilson WE, Goodhead DT (2001) Computational approach for determining the spectrum of DNA damage induced by ionizing radiation. *Radiat Res* 156: 577–583. doi:10.1667/0033-7587(2001)156[0577:cafdts]2.0.co;2.

Noon AT, Shibata A, Rief N, Löbrich M, Stewart GS, Jeggo PA, Goodarzi AA (2010) 53BP1-dependent robust localized KAP-1 phosphorylation is essential for heterochromatic DNA double-strand break repair. *Nat Cell Biol* 12: 177–184. doi:10.1038/ncb2017.

O'Connor TN, Kallenbach JG, Orciuoli HM, Paris ND, Bachman JF, Johnston CJ, Hernady E, Williams JP, Dirksen RT, Chakkalakal JV (2022) Endurance exercise attenuates juvenile irradiation-induced skeletal muscle functional decline and mitochondrial stress. *Skelet Muscle* 12: 022–00291.

Olivé M, Blanco R, Rivera R, Cinos C, Ferrer I (1995) Cell death induced by gamma irradiation of developing skeletal muscle. *J Anat* 187 (Pt 1): 127–132.

Paulino AC (2004) Late effects of radiotherapy for pediatric extremity sarcomas. *Int J Radiat Oncol Biol Phys* 60: 265–274. doi:10.1016/j.ijrobp.2004.02.001.

Pinset C, Montarras D, Chenevert J, Minty A, Barton P, Laurent C, Gros F (1988) Control of myogenesis in the mouse myogenic C2 cell line by medium composition and by insulin: characterization of permissive and inducible C2 myoblasts. *Differentiation* 38: 28–34. doi:10.1111/j.1432-0436.1988.tb00588.x.

Răileanu M, Straticiuc M, Iancu DA, Andrei RF, Radu M, Bacalum M (2022) Proton irradiation induced reactive oxygen species promote morphological and functional changes in HepG2 cells. *J Struct Biol* 214: 107919. doi:10.1016/j.jsb.2022.107919.

Rezaee M, Adhikary A (2024) The Effects of Particle LET and Fluence on the Complexity and Frequency of Clustered DNA Damage. *DNA Basel* 4: 34–51. doi:10.3390/dna4010002.

Rybanska-Spaeder I, Reynolds TL, Chou J, Prakash M, Jefferson T, Huso DL, Desiderio S, Franco S (2013) 53BP1 is limiting for NHEJ repair in ATM-deficient model systems that are subjected to oncogenic stress or radiation. *Mol Cancer Res* 11: 1223–1234. doi:10.1158/1541-7786.mcr-13-0252-t.

Schneider CA, Rasband WS, Eliceiri KW (2012) NIH Image to ImageJ: 25 years of image analysis. *Nat Methods* 9: 671–675. doi:10.1038/nmeth.2089.

Seale P, Asakura A, Rudnicki MA (2001) The potential of muscle stem cells. *Dev Cell* 1: 333–342. doi:10.1016/s1534-5807(01)00049-1.

Shao Z, Davis AJ, Fattah KR, So S, Sun J, Lee KJ, Harrison L, Yang J, Chen DJ (2012) Persistently bound Ku at DNA ends attenuates DNA end resection and homologous recombination. *DNA Repair Amst* 11: 310–316. doi:10.1016/j.dnarep.2011.12.007.

Shibata A, Jeggo PA (2020) Roles for 53BP1 in the repair of radiation-induced DNA double strand breaks. *DNA Repair Amst* 93: 102915. doi:10.1016/j.dnarep.2020.102915.

Siegel RL, Miller KD, Jemal A (2020) Cancer statistics, 2020. *CA Cancer J Clin* 70: 7–30. doi:10.3322/caac.21590.

Sung P, Robberson DL (1995) DNA strand exchange mediated by a RAD51-ssDNA nucleoprotein filament with polarity opposite to that of RecA. *Cell* 82: 453–461. doi:10.1016/0092-8674(95)90434-4.

Sutcu HH, Montagne B, Ricchetti M (2023) DNA-PKcs regulates myogenesis in an Akt-dependent manner independent of induced DNA damage. *Cell Death Differ* 30: 1900–1915. doi:10.1038/s41418-023-01177-2.

Sutcu HH, Rassinoux P, Donnio LM, Neuillet D, Vianna F, Gabillot O, Mari PO, Baldeyron C, Giglia-Mari G (2024) Decline of DNA damage response along with myogenic differentiation. *Life Sci Alliance* 7. doi:10.26508/lsa.202302279.

Toledo LI, Altmeyer M, Rask M-B, Lukas C, Larsen DH, Povlsen LK, Bekker-Jensen S, Mailand N, Bartek J, Lukas J (2013) ATR Prohibits Replication Catastrophe by Preventing Global Exhaustion of RPA. *Cell* 155: 1088–1103. doi:10.1016/j.cell.2013.10.043.

Tuan Anh L, Ngoc Hoang T, Thibaut Y, Chatzipapas K, Sakata D, Incerti S, Villagrasa C, Perrot Y (2024) "dsbandrepair" – An updated Geant4-DNA simulation tool for evaluating the radiation-induced DNA damage and its repair. *Phys Med* 124: 103422. doi:10.1016/j.ejmp.2024.103422.

Vahidi Ferdousi L, Rocheteau P, Chayot R, Montagne B, Chaker Z, Flamant P, Tajbakhsh S, Ricchetti M (2014) More efficient repair of DNA double-strand breaks in skeletal muscle stem cells compared to their committed progeny. *Stem Cell Res* 13: 492–507. doi:10.1016/j.scr.2014.08.005.

Vianna F, Gonon G, Lalanne K, Adam-Guillermin C, Bottollier-Depois J-F, Daudin L, Dugué D, Moretto P, Petit M, Serani L *et al* (2022) Characterization of MIRCOM, IRSN's new ion microbeam dedicated to targeted irradiation of living biological samples. *Nucl Instrum Methods Phys Res Sect B Beam Interact Mater At* 515: 20–30. doi:https://doi.org/10.1016/j.nimb.2022.01.007.

Vitti ET, Parsons JL (2019) The Radiobiological Effects of Proton Beam Therapy: Impact on DNA Damage and Repair. *Cancers Basel* 11. doi:10.3390/cancers11070946.

Wang JJ, Lei KF, Han F (2018) Tumor microenvironment: recent advances in various cancer treatments. *Eur Rev Med Pharmacol Sci* 22: 3855–3864.

Ward IM, Reina-San-Martin B, Olaru A, Minn K, Tamada K, Lau JS, Cascalho M, Chen L, Nussenzweig A, Livak F *et al* (2004) 53BP1 is required for class switch recombination. *J Cell Biol* 165: 459–464. doi:10.1083/jcb.200403021.

Zhang LL, Mao YP, Zhou GQ, Tang LL, Qi ZY, Lin L, Yao JJ, Ma J, Lin AH, Sun Y (2015) The Evolution of and Risk Factors for Neck Muscle Atrophy and Weakness in Nasopharyngeal Carcinoma Treated With Intensity-Modulated Radiotherapy: A Retrospective Study in an Endemic Area. *Med Baltim* 94: e1294. doi:10.1097/md.0000000000001294.

Zhao L, Bao C, Shang Y, He X, Ma C, Lei X, Mi D, Sun Y (2020) The Determinant of DNA Repair Pathway Choices in Ionising Radiation-Induced DNA Double-Strand Breaks. *Biomed Res Int* 2020: 4834965. doi:10.1155/2020/4834965.

Figure legends

Figure 1. Recruitment kinetics of NHEJ factor KU80-GFP to the site of localized α-particle and proton irradiation within nuclei of proliferating myoblasts.

A, B Representative images of KU80-GFP recruitment in stably KU80-GFP-expressing C2C7 myoblasts upon localized irradiation (white arrowhead) with the indicated number of α-particles (A) and protons (B). The irradiation was applied at t = 10 s. Scale bar represents 10μm.

C, D Kinetic curves of KU80-GFP recruitment obtained from A and B upon local irradiation with reducing number of α-particles (C) and protons (D) delivered. Error bars represent the SEM obtained from N= 3 independent experiments with 65 - 210 nuclei / condition analyzed in C and 42 - 175 nuclei / condition analyzed in D. Statistical analysis was performed by using generalized additive models (GAM) framework model and comparing each time point. Dashed boxes represent the region of slopes with significant difference between the kinetic curves. Color code of boxes represents the same color kinetic curve vs curve of highest number of particle irradiation. **** $p < 0.00001$.

Figure 1. Response of DDR protein 53BP1 upon localized α-particle and proton irradiation within nuclei of myoblasts.

A, B Kinetic curves of 53BP1-GFP recruitment in stably 53BP1-GFP-expressing C2C7 myoblasts upon 1,000 and 50 α-particles irradiation (A), or upon 10,000 and 500 protons irradiation (B). N= 3 independent experiments, mean ± SEM from 71 – 109 nuclei / condition analyzed in (A) and 23 - 32 nuclei / condition analyzed in (B). Statistical analysis performed by using GAM framework model and comparing each time point. Dashed boxes represent the region of slopes with significant difference between the kinetic curves. Color code of boxes represents the same color kinetic curve vs curve of highest number of particle irradiation. **** $p < 0.00001$.

C, E Representative images of stably KU80-GFP-expressing proliferative C2C7 myoblasts immunostained with antibodies against 53BP1 and the phosphorylated form of the histone variant H2AX (γH2AX) at the indicated time-points after localized irradiation (white arrowhead) by 1,000 α-particles and 10,000 protons (C), and 1h after localized irradiation (white arrowhead) by 1,000, 200 and 50 α-particles or by 10,000, 2,500 and 500 protons (E). DNA is counterstained with DAPI. Scale bar, 10 μm.

D, F Relative fluorescence intensities of 53BP1 staining at local irradiation sites within nuclei of cells from (C) shown in (D) and from (E) shown in (F). N= 3 independent experiments with 22 - 94 nuclei / condition analyzed in (D) and 31 - 94 nuclei / condition analyzed in (F). Data are presented in scatter dot-plots, representing the relative 53BP1-GFP fluorescence intensities at irradiation sites. Bold bars represent the mean and error bars the standard error of the mean (SEM). Statistical significance is obtained by 1-way ANOVA with post-hoc Tukey's multiple comparison test. p-value are ns $p > 0,05$, * $p < 0.05$, ** $p < 0.01$, *** $p < 0.001$.

Figure 2. DSB repair mechanisms taking role in myoblasts upon α-particle micro-irradiation with reducing number of particles.

A Representative images of nuclear γH2AX pattern at the indicated time-points upon micro-irradiation with 1,000, 200 and 50 α-particles in stably KU80-GFP-expressing C2C7 myoblasts immunolabelled against γH2AX. DNA counterstained with DAPI. Scale bar, 10 μm.

B Mean relative nuclear fluorescence intensities of γH2AX within nuclei of myoblasts from (A) at indicated time-points upon micro-irradiation with the indicated α-particle number. N= 3 independent experiments with 50 - 177 cells / condition analyzed.

C Representative images of stably KU80-GFP-expressing myoblasts immunolabelled against the HR factor RAD51 and γH2AX at the indicated time-points upon irradiation (white arrowhead) with the indicated number of α-particles. DNA counterstained with DAPI. Scale bar, 10 μm.

D, E Mean fluorescence intensities of recruited KU80-GFP (D), and immunostaining with anti-RAD51 antibody (E) at the indicated time-points after micro-irradiation with the indicated number of α-particles. N= 3 independent experiments, with 51 - 164 cells / condition analyzed.

In scatter dot-plots (B, D, E), are represented the relative fluorescence intensities of nuclear γH2AX staining (B) and, KU80-GFP (D) and RAD51 staining (E) at irradiation sites. Bold bars represent the

mean, error bars the SEM. Significance by 2-way ANOVA with post-hoc Tukey's multiple comparison test against the number of α-particles at each indicated time-points. The p-value are ns p> 0,05, * p< 0.05, ** p< 0.01, *** p< 0.001.

Figure 3. DSB repair upon α-particle and proton irradiation.

A - C Mean fluorescence intensities of immunolabelled recruited RAD51 (A), recruited KU80-GFP (B) and immunolabelled total nuclear γH2AX (C) at indicated time-points upon α-particle and proton irradiation. N= 3 independent experiments, with 55 – 177 cells / condition analyzed. Data are presented in scatter dot-plots. Bold bars represent the mean, error bars the SEM. Significance by 2-way ANOVA with post-hoc Sidak's comparison test against the number of particles delivered at each indicated time-points. The p-value are ns p> 0,05, * p< 0.05, ** p< 0.01, *** p< 0.001.

D Representative images (Di) and kinetic curves (Dii) of HP1α-GFP recruitment in C2C7 myoblasts upon 1,000 α-particles and 10,000 protons micro-irradiation. N= 3 independent experiments, mean ± SEM from 30 - 39 cells / condition analyzed.

Figure 5. Different DDR dynamics relying on the characteristics of ionizing charged particles in myoblasts.

Schematic representation (not in scale) of recruitment and release of NHEJ factor (KU80-GFP), HR factor (RAD51), DDR protein (53BP1) and phosphorylation of histone H2AX (γH2AX) and their degree of implications "+ or -" in myoblasts and myotubes upon α-particle (in purple) and proton (in green) micro-irradiation, hence upon different complexities of induced DNA damage (Bertolet et al, 2023; Rezaee & Adhikary, 2024), against time. P.S. decreasing number of particles delivered also followed similar dynamics as for decreased DNA damage complexity (i.e. proton vs α-particle).

Supplementary data

Supplementary materials and methods

Whole cell extracts and immunoblotting

We washed untransfected and stably GFP-tagged protein-expressing C2C7 myogenic cells, both under myoblast and myotube forms, twice in ice-cold PBS. Then, we immediately resuspended and lysed cells in Laemmli buffer containing 50 mM Tris pH 6.8, 2% SDS, 5% glycerol, 2 mM DTT, 2.5 mM EDTA, 2.5 mM EGTA, and 10 mM sodium fluoride (Sigma-Aldrich), supplemented with a cocktail of protease (Complete, EDTA-free tablets; Roche) and phosphatase (ThermoFisher Scientific) inhibitors, as described previously (Maire et al, 2013). Subsequently, we boiled cell lysates at 95 °C for 5 minutes and we then sheared them by syringing through a 26G needle. We quantified the protein concentration by using the BCA Protein Assay Kit-Reducing Agent Compatible (Pierce, ThermoFisher Scientific).

For each extract, we separated 15 µg of protein on a 4-12% TGX gels (BioRad) and transferred onto nitrocellulose membranes (BioRad). We saturated membranes with PBS-T containing 5% skimmed milk powder (Dutsher) and incubated them overnight at 4 °C with the appropriate primary antibodies diluted in TBS-T+ 5% milk. After washes, we incubated membranes with the appropriate HRP peroxidase secondary antibodies for one hour at RT. For visualization of proteins, we incubated membranes with Clarity ECL solution (BioRad) for chemiluminescence detection, imaged and analyzed membranes using the ChemiDoc MP Imaging System (BioRad) and ImageJ software (version 1.53e).

Antibodies

Primary antibodies used during immunoblotting experiments are: rabbit anti-53BP1 (Bethyl, Euromedex, A300-272A; 1:1,000); mouse anti-β-actin (Sigma, A5441; 1:1,000)), which was used as loading control; rabbit anti-H2AX (Cell Signaling Technologies, Ozyme, 2595; 1:1,000); mouse anti-γH2AX (Millipore, UpState, 05-636; 1:2,000); mouse anti-HP1α (Euromedex, 2HP-2G9-AS; 1:1,000); mouse anti- KU80 (Abcam, Ab119935; 1:200); mouse anti-myosine heavy chain (eBioSciences, ThermoFisher Scientific, MF-20, 14-6503-82; 1:500), which was used a marker of myotube state; rabbit anti-PARP1 (Enzo Life Sciences, ALX-210+302; 1:1,000); rabbit anti-RAD51 (Cell Signaling Technologies, Ozyme, 8875; 1:1,000) and β-tubulin (Sigma, TUB 2.1, T4026; 1:1,000), which was also used as loading control.

Secondary antibodies used are: horseradish peroxidase-conjugated affinity-purified donkey anti–mouse or anti–rabbit (1:5,000; Jackson ImmunoResearch Laboratories).

Quantitative Image-Based Cell Cycle Analysis by Epifluorescence Microscopy

In order to determine how irradiated cells progress through the cell cycle, we reacquired the same samples (see “Immunostaining and image acquisition” paragraph of Materials and methods) on an inverted epifluorescence Olympus IX81 SCAN IM IX2 stage (Märzhäuser, Wetzlar, Germany), a MT20 fluorescence illumination microscope with a 10×/0.25 NA objective. The microscope is coupled with a motorized system with a fast filter wheel and an Orca R2 CCD camera (Hamamatsu, Massy, France). We adjusted the acquisition times for the different channels to obtain images under non-saturating conditions (i.e., in the 12-bit dynamic range) for all the experimental points analyzed. After acquisition, we performed image analysis with the Scanˆ R analysis 4.2.1 software (Olympus, Rungis, France), as described previously (Toledo et al, 2013; Gruel et al, 2016). Briefly, we used an edge segmentation algorithm implemented in the software, which is based on Canny’s method to detect nuclei in the DAPI channel (main object) and γH2AX signal in the Texas Red channel (sub-object). We performed a first selection based on the area and circularity of the nuclei to consider only isolated nuclei and to remove from the analysis objects corresponding to clusters of nuclei and cellular debris. As in a flow-cytometry analysis, the cells were distributed in different phases of the cell cycle by assessing the integrated intensity of the DAPI signal (DNA content) within the entire nucleus. We visually determined the region containing the irradiated myoblasts through the γH2AX signal. Finally, we determined the cell cycle stage of all irradiated myoblasts together and non-irradiated myoblasts for each time-point upon irradiation to be able to analyze a minimum number of nuclei.

Statistical analyses

The data shown result from at least two independent experiments.

In order to investigate the impact of the experimental conditions on each monocellular fluorescence intensities, we performed a partial least squares discriminant analysis (PLS-DA) on the monocellular GFP-KU80 recruitment, RAD51, and γH2AX signals for the classification of groups defined by their type and number of particles as well as their time-points post-irradiation. The PLS-DA is a supervised dimension approach aiming to project a given dataset (here the fluorescence intensity matrices) on a subspace optimally separated according to a categorical variable (here the experimental conditions). Similarly, to its unsupervised dimension reduction counterpart, the well-known principal component analysis (PCA), the interpretation of PLS-DA consists on examining the contribution of the original covariates in the construction of its dimension components (called loadings).

Supplementary Table

	LET (keV/µm)	Mean EDep (keV)	Nb particle	Mean Dose/dot (Gy)	Nb sDSB	Nb cDSB
4 MeV Proton	10 keV.µm^{-1}	35,04				
			500	7,2	**57,2**	**8,6**
			2,500	35,9	**285,9**	**43,0**
			10,000	143,4	**1143,8**	**172,1**
6 MeV α-particle	84 keV.µm^{-1}	346,2				
			50	7,1	**109,7**	**71,9**
			200	28,3	**438,9**	**287,6**
			1,000	141,7	**2194,3**	**1438,2**

Table S1- Estimated number of simple DNA double strand breaks (sDSB) and complex DSB (cDSB, defined as 1 DSB + 1 or more strand breaks) for irradiations at a single dot within myoblast nuclei by defined number of 4 MeV proton or 6 MeV α-particle.

These estimations were obtained from “dsbandrepair”, a Geant4-DNA simulation tool (Meylan et al, 2017; Tuan Anh et al, 2024) based on an extrapolation of experimental data from fibroblasts to those from myoblasts. This tool also estimates the mean energy deposit (Mean EDep) for each particle and the mean dose absorbed at the localized irradiation site.

Supplementary figure legends

Figure S1. Characterization of myogenic C2C7 cells expressing GFP-fused proteins.

A, B Immunoblot analysis of GFP-tagged proteins produced by myogenic C2C7 cells stably transfected. Whole cell extracts of myogenic cells at the state of myoblast and myotube were probed with specific antibodies against 53BP1, KU80 and HP1α (upper panels) or with an anti-GFP antibody (bottom panels) (A) or against others DDR proteins, as PARP1, RAD51 and γH2AX (B). The positions of endogenous and GFP-tagged proteins are indicated in (A). * indicates in 53BP1-GFP-expressing myogenic cells the presence of truncated 53BP1-GFP proteins at a very low signal level. Actin and tubulin are used as loading control in (A, B) and myosin heavy chain as marker of myotube state in (B). The sizes of protein molecular weight markers (MW) are indicated in kDa. The immunoblots presented here are representative of 4 independent experiments.

Figure S2. Kinetic curves of KU80-GFP recruitment to the site of α-particle and proton micro-irradiation within myonuclei of differentiated myotubes.

A, B Representative images of KU80-GFP recruitment in stably KU80-GFP-expressing C2C7 myotubes upon localized irradiation with reducing number of α-particles delivered (A) or protons (B). The localized irradiation site is marked with white arrowhead. Scale bar represents 10 µm.

C, D Kinetic curves of KU80-GFP recruitment obtained from A and B upon localized irradiation with a reducing number of α-particles (C) and protons (D). Error-bars represent the SEM obtained from N= 3 independent experiments with 46 - 85 nuclei / condition analyzed in (C) and 12 - 67 nuclei / condition analyzed in (D). The kinetic curves of KU80-GFP recruitments obtained in C2C7 myoblasts (Fig. 1) are also shown only for the irradiation with highest number of particles (i.e., 1,000 α-particles in (C) and 10,000 protons in (D)) by a very light blue curve. Statistical analysis performed by using generalized additive models (GAM) framework model and comparing each time point. Dashed boxes represent the region of slopes with significant difference between the kinetic curves. Color code of boxes represents the same color kinetic curve vs curve of highest number of particle irradiation. **** $p < 0.00001$.

E Quantification of KU80-GFP protein expression level by direct IF during myogenic differentiation, in C2C7 myoblasts (MB) and their committed progeny, myotubes (MT). The measured GFP fluorescence intensity of KU80-GFP in myoblasts and myotubes are presented in scatter dot-plots, with bold bars representing the mean and error bars the standard error of the mean (SEM) from at least 120 nuclei/cell type and data are representative of three independent experiments. Significance by unpaired t-Test, with ns for $p > 0,05$.

Figure S3. Accumulation of 53BP1 upon localized α-particle and proton irradiation in post-mitotic myotubes.

A Recruitment kinetics of 53BP1-GFP in stably 53BP1-GFP-expressing C2C7 myotubes upon 1,000 and 50 α-particles or 10,000 protons irradiation. N= 3 independent experiments, mean ± SEM from 12 - 38 nuclei / condition analyzed. Statistical analysis performed by using GAM framework model and comparing each time point. Dashed boxes represent the region of slopes with significant difference between the kinetic curves. Color code of boxes represents the same color kinetic curve vs curve of highest number of particle irradiation. **** $p < 0.00001$.

B Quantification of 53BP1-GFP protein expression level by direct IF during myogenic differentiation, in C2C7 myoblasts (MB) and myotubes (MT). The measured GFP fluorescence intensity of 53BP1-GFP in myoblasts and myotubes are presented in scatter dot-plots, with bold bars representing the mean and error bars the SEM from at least 120 nuclei/cell type and data are representative of three independent experiments. Significance by unpaired t-Test, with ns $p > 0,05$.

C Relative fluorescence intensities at the site of localized irradiation of 53BP1 revealed by immunostaining at the indicated time upon targeted irradiation by 1,000 α-particles of stably KU80-GFP-expressing myocytes and myotubes. N= 3 independent experiments with 21 - 122 nuclei / condition analyzed. Data are presented in scatter dot-plots with bold bars representing the mean and error bars the SEM. Statistical significance is obtained by 2-way ANOVA with post-hoc Tukey's multiple comparison test between myocytes and myotubes, with ns $p > 0,05$, * $p < 0.05$, ** $p < 0.01$, *** $p < 0.001$.

D Representative images of stably KU80-GFP-expressing myocytes (MC) and myotubes (MT) from (B) immunostained with antibodies against 53BP1 and γH2AX at the indicated time-points upon localized irradiation by 1,000 α-particles. DNA counterstained with DAPI. Scale bar, 10 µm.

Figure S4. Balance between NHEJ and HR.

A, B Mean nuclear fluorescence intensities of γH2AX staining (A) and, RAD51 staining and KU80-GFP signal (B) within nuclei of stably KU80-GFP-expressing C2C7 myoblasts at localized irradiation site 1 h after α-particles micro-irradiation with a reducing number of particles delivered. N= 3 independent experiments with 38 - 177 cells / condition analyzed. Data are presented in scatter dot-plots with bold bars representing the mean and error bars the SEM. Significance by 1-way (A) and 2-way (B) ANOVA with post-hoc Tukey's multiple comparison test against the number of particles targeted. significant p-value are ns $p > 0,05$, * $p < 0.05$, ** $p < 0.01$, *** $p < 0.001$.

C, D Cell cycle distribution of non-irradiated neighboring myoblasts (C) and targeted myoblasts (D) upon irradiation with α-particles (Di) or protons (Dii), analyzed by immunofluorescence. Each value shown represents the mean of at least two independent irradiations. For each value, we analyzed in total between 80 and 800 nuclei. The error bars represent the standard error, and the p values are indicated (* $p < 0.05$).

Figure S5. Diversification of C2C7 myoblasts depending on the fluorescence intensities of RAD51 and γH2AX staining and KU80-GFP signal upon micro-irradiation with α-particles targeted over time.

A, B The partial least squares discriminant analysis (PLS-DA) scatterplots of data from Fig. S3 and Fig. 3, B-E according to the numbers of α-particles delivered (A), and according to the periods of time post-IR (B). The PLS-DA results in panels A-B were obtained from the α-particles dataset (986 cells). The significant contribution of RAD51, KU80 (KU80-GFP) and γH2AX intensities provided by the PLS-DA loading weight analysis are indicated with "+" symbol for each group.

C, D The position of each group of data from PLS-DA (A, B) are represented by density plots (in red) according to the numbers of α-particles delivered (C), and according to the periods of time post-IR (D).

E The performance measurement of the separation of each group of data from PLS-DA to other conditions is estimated by the aera under the curves. The AUC and the p value for each classification are shown in table.

Figure S6. Diversification of C2C7 myoblasts depending on the fluorescence intensities of RAD51 and γH2AX staining and KU80-GFP signal upon micro-irradiation with protons targeted over time.

A, B PLS-DA scatterplots of data upon irradiation with 10,000 protons, from Fig. 4, A-C, against α-particle irradiation with different number of particles from Fig. S5, A (A) and then over period of time post-IR from Fig. S5, B (B). The PLS-DA results in panels A-B were obtained from the α-particles and protons merged datasets (986 and 183 cells respectively). The significant contribution of RAD51, KU80 (KU80-GFP) and γH2AX intensities provided by the PLS-DA loading weight analysis are indicated with "+" symbol for each group.

C, D The position of each group of data from PLS-DA (A, B) are represented by density plots (in red) according to the numbers of α-particles or protons delivered (C), and according to the periods of time post-IR (D).

E The performance measurement of the separation of each group of data from PLS-DA to other conditions is estimated by the aera under the curves. The AUC and the p value for each classification are shown in table.

Supp. References

Gruel G, Villagrasa C, Voisin P, Clairand I, Benderitter M, Bottollier-Depois J-F, Barquinero JF (2016) Cell to Cell Variability of Radiation-Induced Foci: Relation between Observed Damage and Energy Deposition. *PLOS ONE* 11: e0145786. doi:10.1371/journal.pone.0145786.

Maire V, Baldeyron C, Richardson M, Tesson B, Vincent-Salomon A, Gravier E, Marty-Prouvost B, De Koning L, Rigaill G, Dumont A *et al* (2013) TTK/hMPS1 Is an Attractive Therapeutic Target for Triple-Negative Breast Cancer. *PLoS ONE* 8: e63712. doi:10.1371/journal.pone.0063712.

Meylan S, Incerti S, Karamitros M, Tang N, Bueno M, Clairand I, Villagrasa C (2017) Simulation of early DNA damage after the irradiation of a fibroblast cell nucleus using Geant4-DNA. *Sci Rep* 7: 11923. doi:10.1038/s41598-017-11851-4.

Toledo LI, Altmeyer M, Rask M-B, Lukas C, Larsen DH, Povlsen LK, Bekker-Jensen S, Mailand N, Bartek J, Lukas J (2013) ATR Prohibits Replication Catastrophe by Preventing Global Exhaustion of RPA. *Cell* 155: 1088–1103. doi:10.1016/j.cell.2013.10.043.

Tuan Anh L, Ngoc Hoang T, Thibaut Y, Chatzipapas K, Sakata D, Incerti S, Villagrasa C, Perrot Y (2024) "dsbandrepair" – An updated Geant4-DNA simulation tool for evaluating the radiation-induced DNA damage and its repair. *Phys Med* 124: 103422. doi:10.1016/j.ejmp.2024.103422.

Sutcu et al., Figure 1

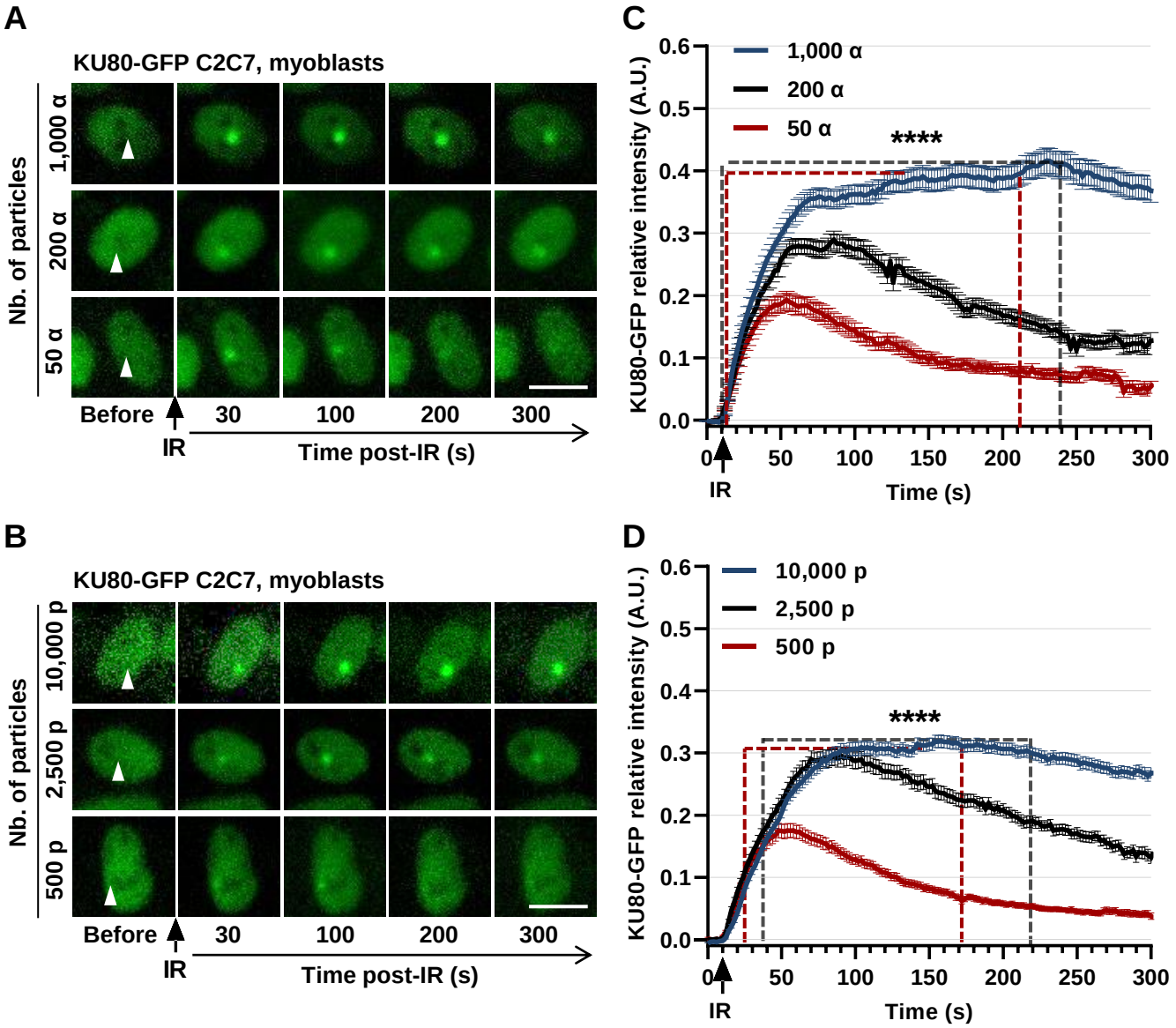

Sutcu et al., Figure 2

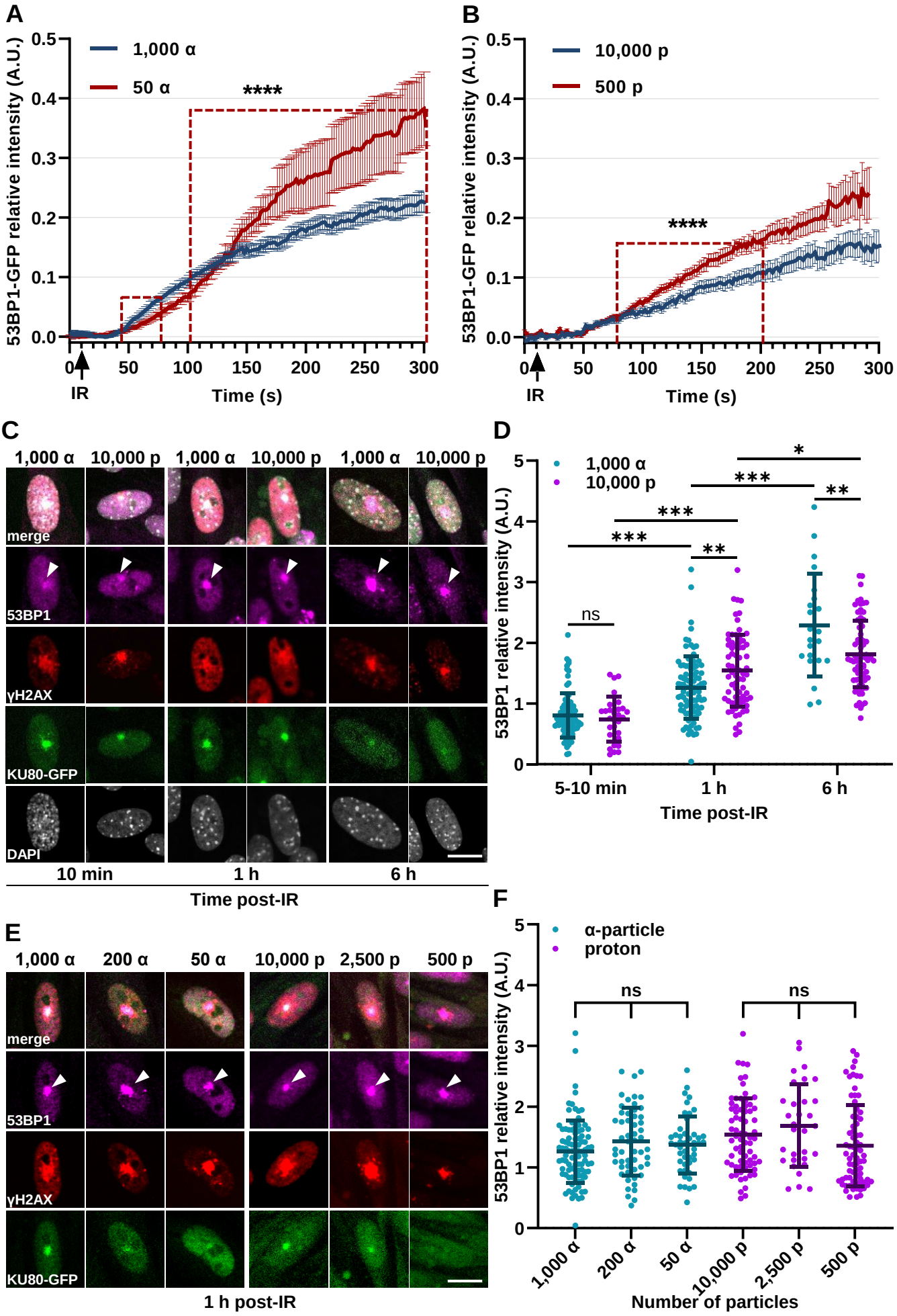

Sutcu et al., Figure 3

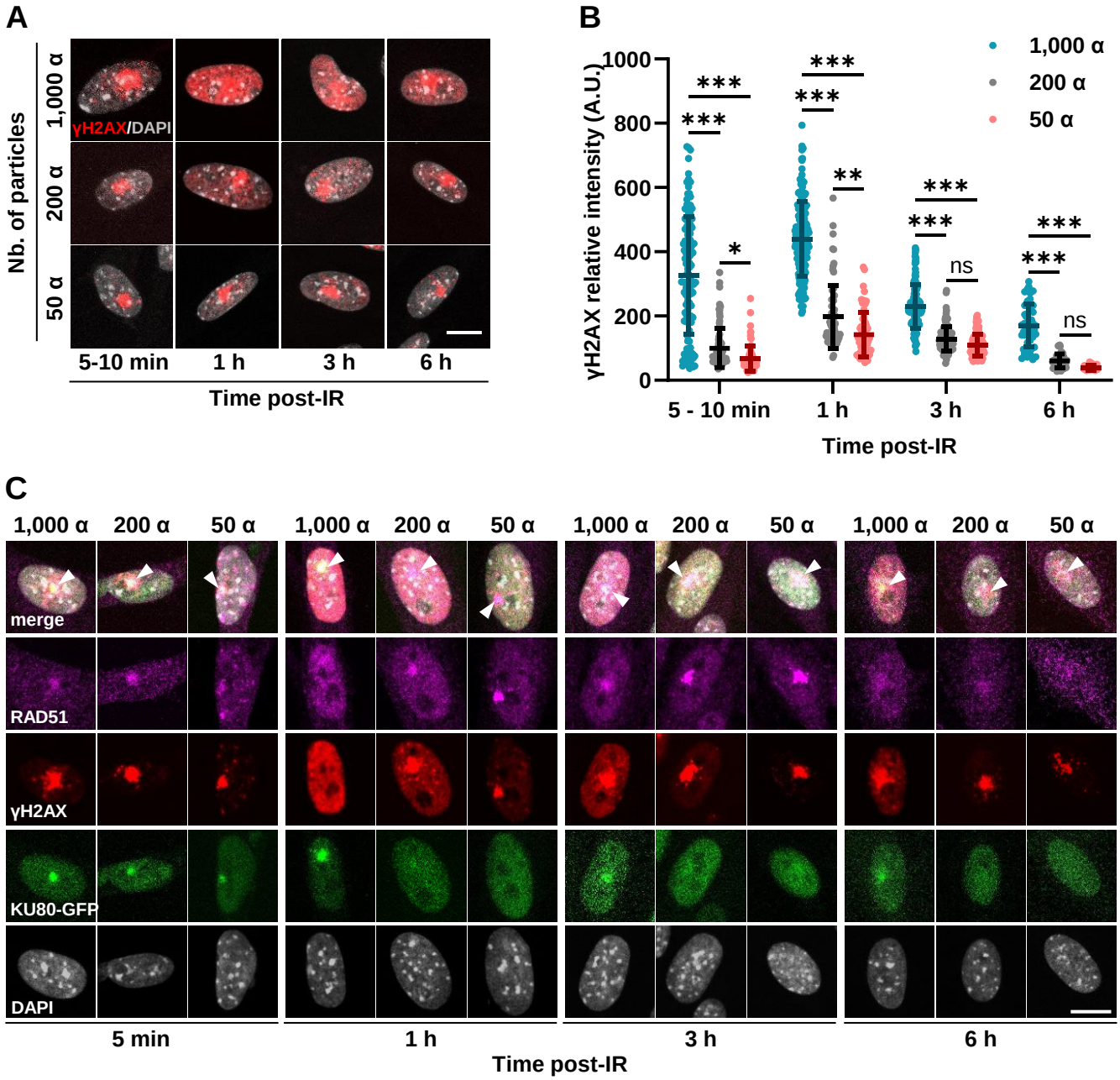

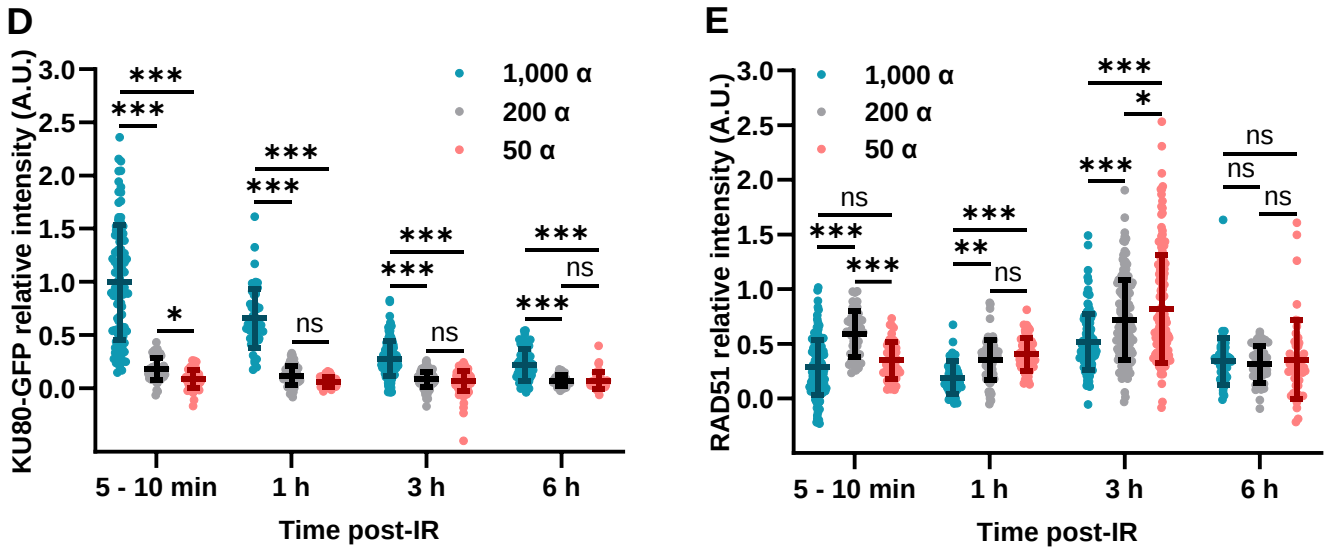

Sutcu et al., Figure 4

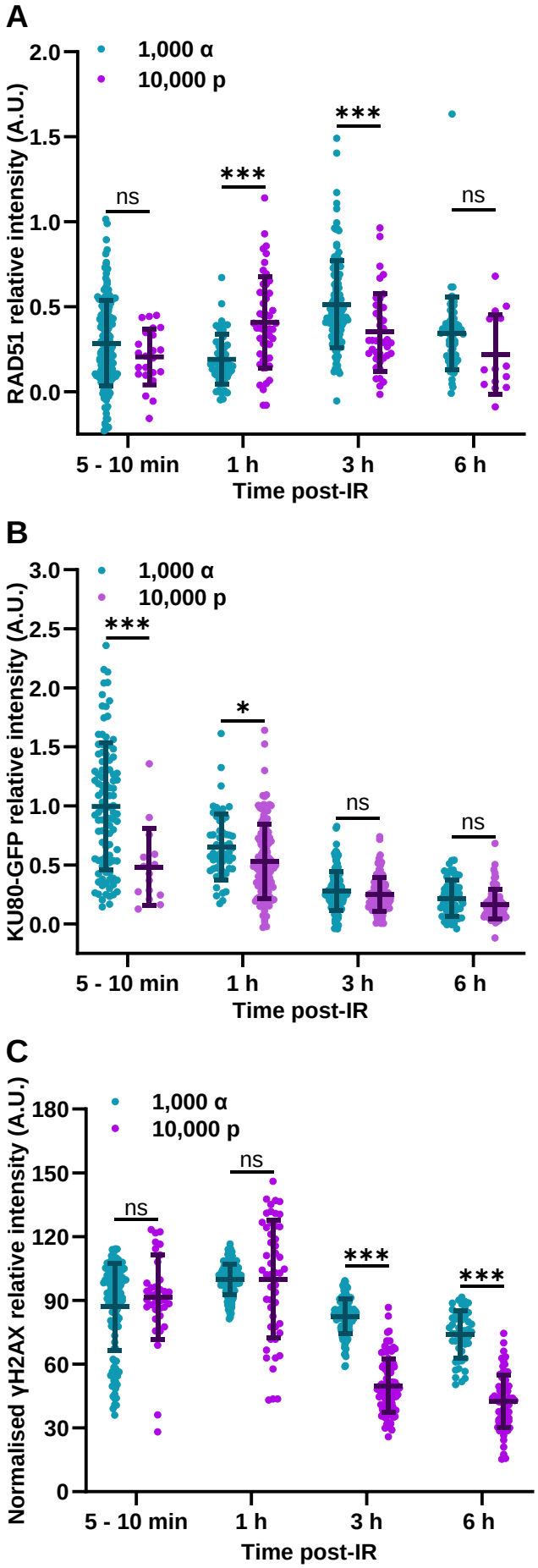

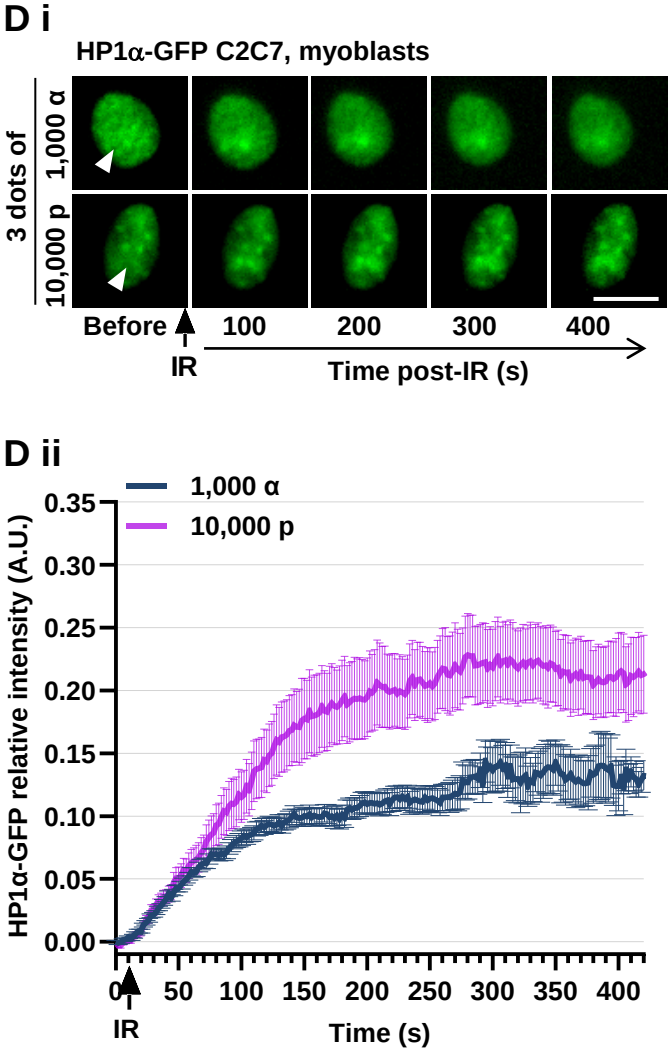
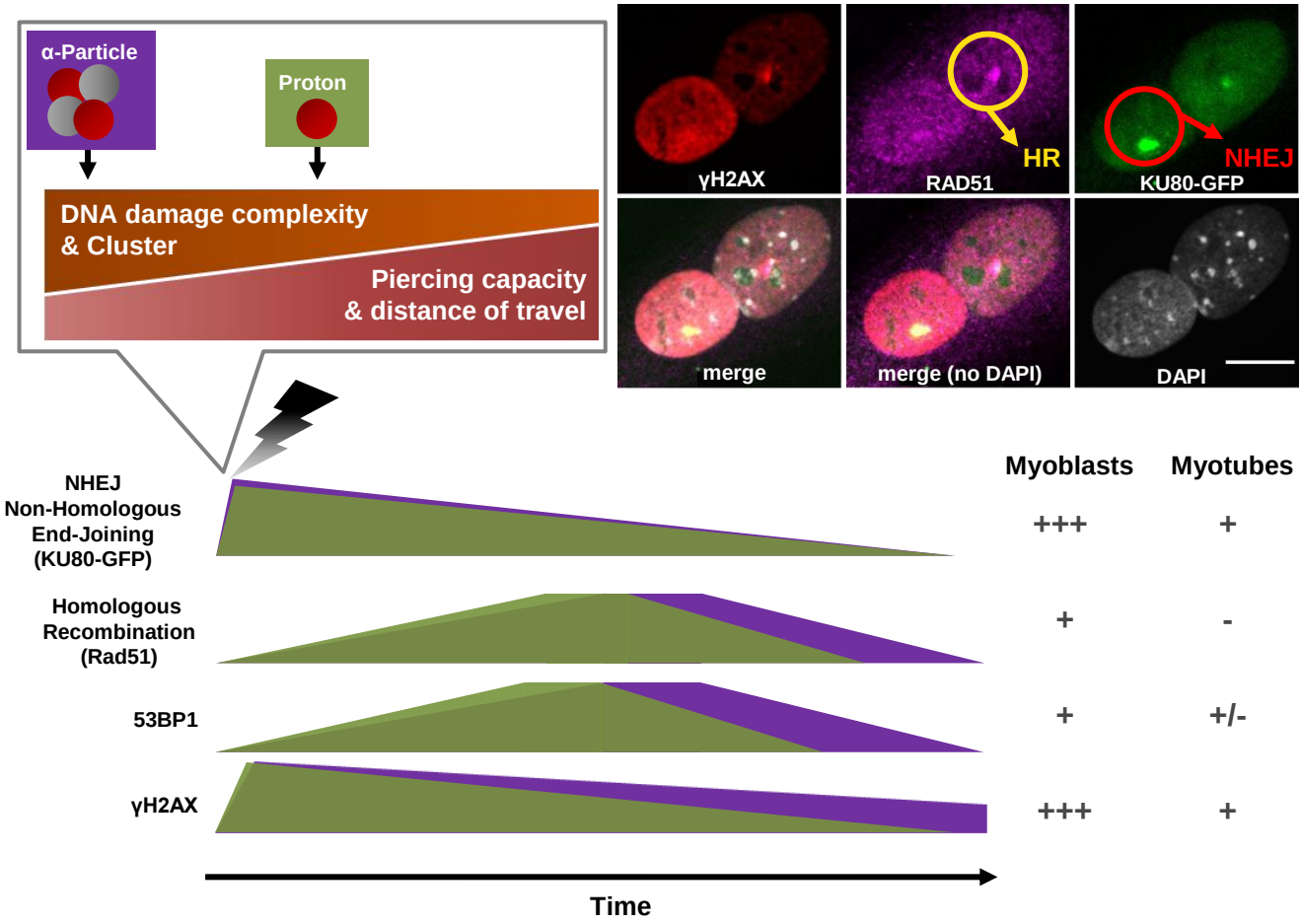
Sutcu et al., Figure 5